MNRAS 000, 1–20 (2022) Preprint 26 July 2022 Compiled using MNRAS LATEX style file v3.0

Simulating the shock dynamics of a neutron star accretion column

Pavel Abolmasov,[1,2]★ Galina Lipunova,[3]
[1]The Raymond and Beverly Sackler School of Physics and Astronomy, Tel Aviv University, Tel Aviv 69978, Israel
[2] Department of Physics and Astronomy, FI-20014 University of Turku, Finland
[3]Sternberg Astronomical Institute, Moscow State University, Universitetsky pr. 13, 119234 Moscow, Russia

Accepted XXX. Received YYY; in original form ZZZ

ABSTRACT

Accretion onto a highly-magnetised neutron star runs through a magnetospheric flow, where the plasma follows the magnetic field lines in the force-free regime. The flow entering the magnetosphere is accelerated by the gravity of the star and then abruptly decelerated in a shock located above the surface of the star. For large enough mass accretion rates, most of the radiation comes from the radiation-pressure-dominated region below the shock, known as accretion column. Though the one-dimensional, stationary structure of this flow has been studied for many years, its global dynamics was hardly ever considered before. Considering the time-dependent structure of an accretion column allows us to test the stability of the existing stationary analytic solution, as well as its possible variability modes, and check the validity of its boundary conditions. Using a conservative scheme, we perform one-dimensional time-dependent simulations of an ideal radiative MHD flow inside an aligned dipolar magnetosphere. Whenever thermal pressure locally exceeds magnetic pressure, the flow is assumed to lose mass. Position of the shock agrees well with the theoretical predictions below a limit likely associated with advection effects: if more than $2/3$ of the released power is advected with the flow, the analytic solution becomes self-inconsistent, and the column starts leaking at a finite height. Depending on the geometry, this breakdown may broaden the column, mass-load the field lines, and produce radiation-driven, mildly relativistic ejecta. Approaching the equilibrium position, the shock front experiences damped oscillations at a frequency close to the inverse sound propagation time.

Key words: stars: neutron – stars: magnetic field – X-rays: binaries – methods: numerical

1 INTRODUCTION

Depending on their nature and fundamental parameters, compact objects may gain matter via different types of accretion flows. In particular, for a strongly magnetised neutron star (NS), magnetic field is an important factor shaping the innermost parts of the flow. Close to the star, magnetic stresses may dominate the momentum balance, and the matter is forced to follow the field lines and, in particular, to co-rotate with the NS. Such objects normally manifest themselves as X-ray pulsars (XRPs), hard X-ray sources showing coherent flux pulsations with the spin period of the star (e. g. Caballero & Wilms 2012; Wolff et al. 2019; Mushtukov & Tsygankov 2022). For most XRPs, the size of the magnetosphere replacing the disrupted inner portions of the accretion disc is normally two-three orders of magnitude larger than the size of the accreting neutron star (NS). Given the shape of the potential well, this means that practically all the energy of the accretion flow is released deep inside the magnetosphere. Hence, modelling the magnetospheric part of the flow is crucial for the understanding of the observational properties of XRPs and their long-time evolution.

XRPs are historically known as a subclass of high-mass X-ray binaries. Most of the well-studied XRPs are binaries consisting of a NS with a massive Be-star companion (Bildsten et al. 1997; Raguzova & Popov 2005). Rapid rotation of the donor stars, large eccentricities and misalignment of many of these systems lead to complicated mass transfer rate variation patterns with different types of flares and orbital and super-orbital variability (Reig 2011). Less numerous but important classes of XRPs include systems with OB-supergiant donor stars (like Vela X-1, see Kretschmar et al. 2021 for review) and intermediate-mass subgiant donors (like Her X-1, see for example Brumback et al. 2021). Recently, new classes of XRPs were discovered: accreting millisecond X-ray pulsars (see Patruno & Watts 2021 for a review) and super-Eddington pulsating ultraluminous X-ray pulsars (Bachetti et al. 2014).

Ultraluminous X-ray sources (ULXs) are known since 1980-s as a population of extragalactic X-ray sources exceeding the Eddington limit for a conventional black hole (about 10^{39} erg s^{-1}; see Kaaret et al. 2017 for a review). They were usually identified as either intermediate-mass black holes in binary systems (Portegies Zwart et al. 2004) or stellar-mass black holes accreting at super-Eddington rates (Poutanen et al. 2007). But, intriguingly, during the last few years, several known ULXs were found to produce strong coherent pulsations in the X-ray range (Bachetti et al. 2014; Fürst et al. 2016; Israel et al. 2017a,b; Rodríguez Castillo et al. 2020). The simplest way to explain the pulsations is by an anisotropically-emitting rotating NS. Spectral properties of many other ULXs are close to the properties of pulsating ULXs (PULX), suggesting an even larger population of supercritically accreting NSs (Pintore et al. 2017). PULX may be considered as XRPs accreting at super-Eddington rates, though a debate is going on about the role of geometric or relativistic beaming

★ E-mail: pavel.abolmasov@gmail.com

in these objects (see, for instance, Abarca et al. 2021 and Mushtukov et al. 2021).

Conventional model of an XRP involves an accretion disc around the NS, a magnetosphere that replaces the inner parts of the disc, and a compact region near the surface of the star where most of the radiation is produced. Usually, a NS is assumed to have a dipolar magnetic field. However, a pure dipole cannot coexist with the accretion disc outside the outer boundary of the magnetosphere, hence the magnetic field lines are divided into open lines, closed lines (retaining dipole topology), and mass-loaded lines strongly interacting with the disc. This picture was proposed in early analytical works (e.g. Scharlemann 1978) and is in general supported by numerical simulations (Kulkarni & Romanova 2013; Parfrey & Tchekhovskoy 2017). The accretion flow is confined to two narrow flux tubes connecting the inner rim of the disc to the ring- or crescent-shaped regions near the magnetic poles of the NS (Bachetti et al. 2010; Kulkarni & Romanova 2013). Gravitational energy of the matter falling along the magnetic field lines is converted to kinetic energy, and then to heat and to radiation in a shock wave located either very close to the surface of the NS (the hot spot case), or above the surface of the star, if the radiation pressure contribution is large (Davidson 1973; Inoue 1975; Basko & Sunyaev 1976). The latter case, associated with higher luminosities, is usually described as an *accretion column*.

A detailed analytic model of a radiation-pressure-supported accretion column was developed by Basko & Sunyaev (1976) (hereafter BS). Referring to BS, we will always address their 'sinking regime' described in section 4.4 of their paper, that is, the case relevant for a geometrically high, radiation-pressure-supported accretion column. The minimal luminosity required for the formation of a column is less than the Eddington luminosity, as the accretion flow, channelled by the magnetic field lines, is confined to a small fraction of the NS surface. The heat in an accretion column is mainly produced by adiabatic heating and is radiated away by the sides of the flow. The model developed by BS recovers the structure of the accretion flow downstream of the shock and determines the position of the shock as an eigenvalue of the problem.

The approximation used by BS involved several assumptions, including simplified geometry, stationarity, Newtonian physics, fixed and isotropic scattering cross-section, absence of radial heat diffusion, domination of radiation pressure, and a certain set of boundary conditions at the surface of the NS. At the surface of the star, the mass flux is the same as the mass accretion rate at the outer boundary, and the pressure is equal to the magnetic field pressure, meaning the footpoints of the magnetic field lines are at the edge of a breakdown. The boundary condition for the pressure provides a physical explanation for what might seem to be a violation of mass conservation in the model: the pressure at the base of the column is large enough to squeeze the accreting matter sideways by displacing the magnetic field lines. The actual physics responsible for the 'leakage' of the column is likely some kind of interchange instability that arises when thermal pressure becomes comparable to magnetic field pressure or exceeds the latter by some factor (Litwin et al. 2001; Mukherjee et al. 2013; Kulsrud & Sunyaev 2020).

In more recent studies, some of these assumptions were relaxed. For instance, in the paper by West et al. (2017a), the structure of the column is treated in an inclined dipolar geometry, including realistic opacities and detailed energy transfer between electrons, ions, and radiation. The papers including elaborate microphysics and radiative transfer (Becker 1998; Becker & Wolff 2007; West et al. 2017a) are complemented by large-scale two- and three-dimensional simulations of accreting magnetospheres (Wang & Frank 1981; Arons et al. 1987; Kulkarni & Romanova 2013; Kawashima et al. 2016), that provide important insights into the global structure of the flow.

Here, we aim to relax some of the assumptions of BS, and, first of all, the assumption of stationarity. This might be important because the mass accretion rates in real XRPs are highly variable on multiple time scales, some of which (such as dynamic and sometimes viscous time scales of the inner accretion disc) are shorter than the time needed for the column to approach equilibrium (see section 2.2). Considering a time-dependent problem would allow us to see the formation of the shock and its evolution towards the equilibrium position.

Besides, time-dependent treatment allows us to check the analytic stationary model of BS for consistency. In particular, we can check if their boundary condition at the surface of the star is a natural outcome of the time-dependent evolution. Force-free accretion onto a solid-surface NS leads to accumulation of mass and heat inside the column. This, in turn, likely leads to a breakdown of the force-free assumption when thermal pressure starts exceeding magnetic stresses. If this happens near the bottom of the column, the stationary picture proposed by BS would be naturally reproduced. However, as the magnetic field pressure drops with radius $\propto R^{-6}$, and the thermal pressure may easily (as we will show later in section 3.4) have a shallower profile in particular circumstances such as strong advection in the flow, we expect a different scenario to be realised for certain combinations of parameters.

In the analytic model by BS, increase of the mass accretion rate shifts the shock wave upwards, towards the accretion disc. Applied to PULXs, the model predicts either a shock located very high in the magnetosphere, or a completely subsonic optically thick flow similar to the scenario proposed by Mushtukov et al. (2017). Extending the solution so far into the magnetosphere requires taking into account additional effects such as irradiation (outer regions of the flow intercept significant part of the luminosity generated by its inner parts), centrifugal force, and more complex geometry (dipole is no more consistent with a power-law approximation). Apart from this, as we will see in section 3.3, self-consistency of the analytic model is limited by advection effects that become important for large mass accretion rates and small radiating surfaces of the column.

An important question that has hardly ever been addressed in the case of NSs is whether accretion columns have observable global oscillation modes. This is potentially a very important issue, because any oscillations formed near the surface of the star are direct probes of its properties: strong gravity, magnetic fields, and the physical conditions in the flow.

Apparently, there is no unambiguous observational evidence for any oscillation modes coming from accretion columns. Normally, the power density spectrum (PDS) of an XRP shows a broad-band noise with a break at some frequency positively correlated with the flux (Revnivtsev et al. 2009). The break frequency is close to the expected Keplerian frequency at the boundary between the magnetosphere and the disc, and the observed correlation reasonably fits into the concept of the magnetosphere size changing with the accretion rate (see, e.g., Pringle & Rees 1972; Lamb et al. 1973; Bildsten et al. 1997; Filippova et al. 2017). However, at large, super-Eddington, luminosities, the PDS acquires an additional broad-band noise component peaking at about the break frequency (Revnivtsev et al. 2009; Reig & Nespoli 2013). One of the proposed explanations is the presence of oscillations in the outer parts of the magnetospheric flow. The possible sources of the oscillations could be the feedback from the irradiation by the inner, bright parts of the flow, or a combination of the centrifugal force, radiation, and gravity. One such solution in-

volving low-optical-depth matter trapped in the magnetosphere was proposed by Abolmasov & Biryukov (2020).

At higher frequencies (closer to the dynamic frequencies near the surface of the star) most XRPs lack detectable variability. There are however two notable exceptions which will be discussed in this paper (see section 4.2). One is GRO J1744−28 (Klein et al. 1996), where a significant power excess at tens of Hz is observed. The frequency range of the noise is suggestive of the dynamical time scale of the accretion column in this object. Another example is Cen X-3, for which Jernigan et al. (2000) detected a broad, low-quality-factor feature at about 1 kHz (see, however, Revnivtsev et al. 2015). Both cases are explained by the authors as manifestations of the photon-bubble instability. In this paper, we show that similar observational features may be reproduced by global oscillations of the accretion column.

The structure of the paper is as follows. We formulate the problem, write down the equations, and describe the numerical code in section 2. In section 3, we present the results including velocity profiles, shock positions, and variability patterns. We discuss the results in section 4, and conclude in section 5.

2 PROBLEM FORMULATION AND NUMERICAL SETUP

We consider the dynamics of a flow restricted by the aligned dipolar magnetic field of the NS. Motion along the magnetic field lines is affected by gravity, pressure gradients, centrifugal force, and radiation pressure. We use one-dimensional time-dependent approach, assuming the accretion flow uniformly fills a flux tube. Within the tube, all the physical parameters depend only on time and the coordinate along the field line. We use the laws of conservation of mass (continuity equation), momentum (Euler equation projected along the field line), and energy. The code is freely available at `https://github.com/pabolmasov/HACol`.

2.1 Geometry

Figure 1 shows the adopted geometry of the problem. The simulated flow is a pair of symmetric flux tubes, restricted by the surfaces $\theta = \mathrm{const}$ and $\varphi = \mathrm{const}$, starting in the accretion disc and ending on the surface of the NS. The field lines are the lines of an unperturbed magnetic dipole. We use a spherical coordinate grid: radius R, polar angle θ, and azimuthal angle φ. For a single field line, radial coordinate $R = R_\mathrm{e}\sin^2\theta$, where R_e is the equatorial size of the magnetosphere. By the order of magnitude, the size of the magnetosphere is equal to the Alfvén radius

$$R_\mathrm{A} = \left(\frac{\mu^2}{2\dot{M}\sqrt{2GM_*}}\right)^{2/7}. \tag{1}$$

Here, $\dot{M}$ is the mass accretion rate, μ is the magnetic moment of the NS, M_* is the mass of the NS. We normalise the size of the magnetosphere as $R_\mathrm{e} = \xi_\mathrm{m} R_\mathrm{A}$ and set $\xi_\mathrm{m} = 0.5$ in all our models.

For two field lines having slightly different equatorial radii close to R_e and separated at the equator by $\Delta R_\mathrm{e} \ll R_\mathrm{e}$, the distance between the field lines δ is expressed through the polar angle as (see Appendix A):

$$\delta = \frac{R\sin\theta}{\sqrt{1+3\cos^2\theta}}\frac{\Delta R_\mathrm{e}}{R_\mathrm{e}}. \tag{2}$$

Here, ΔR_e has the physical meaning of the penetration depth of the magnetic field into the accretion disc (see Fig. 1). Relatively small value of ΔR_e is a consequence of the high conductivity of the plasma and is reproduced by numerical simulations (Parfrey et al. 2016; Romanova et al. 2003).

A thin (in the sense of $\delta \ll R$) flow has a cross-section of

$$A_\perp = 2\,\delta\, 2\pi a R\sin\theta = 4\pi a R_\mathrm{e}\Delta R_\mathrm{e}\frac{\sin^6\theta}{\sqrt{1+3\cos^2\theta}}. \tag{3}$$

We assume that in the azimuthal direction, the flow occupies a fixed fraction a of the full circle $2\pi R\sin\theta$, with $0 < a \leq 1$. In the absence of strict axisymmetry, the flow is expected to occupy only a limited range of azimuthal coordinates. We treat the cross-section as rectangular, with the perimeter equal to

$$\Pi = 2\left(\frac{A_\perp}{\delta} + 2\delta\right), \tag{4}$$

where the first factor of 2 (as well as the first multiplier 2 in equation 3) comes from the flow actually consisting of two streams accreting onto the two poles of the dipole. Taking into account the lateral sides of the flow (the second term in equation 4) increases the surface of the column by a factor $1 + 2\delta^2/A_\perp$.

As an independent variable for calculations, it is convenient to use a coordinate along the field line, defined as (see equation A3):

$$l = \int \frac{\sqrt{3\cos^2\theta+1}}{2\cos\theta}\,\mathrm{d}R = R_\mathrm{e}\int\sqrt{3\cos^2\theta+1}\,\sin\theta\,\mathrm{d}\theta\,. \tag{5}$$

As both variables, R and θ, increase monotonically along the field line, conversion between l, R, and θ is unique and straightforward.

2.2 Time scales

For each radius R, there is a characteristic dynamical time

$$t_\mathrm{d}(R) = 2\pi\sqrt{\frac{R^3}{GM_*}}. \tag{6}$$

At the surface of the NS, it is of the order $t_\mathrm{d}(R_*) \sim 10^{-4}$s. At the outer edge of the magnetosphere, it can reach the values of seconds, or even larger, for strong enough magnetic fields or small mass accretion rates.

In section 3.6 we will also discuss the sound propagation time scale t_s along the field line

$$t_\mathrm{s} = \int\frac{\mathrm{d}l}{c_\mathrm{s}}, \tag{7}$$

where c_s is the speed of sound. This time depends on the structure of the column, and may be longer (because of sub-virial speed of sound) as well as shorter (when the height of the column is small compared to R_*) than local dynamical times.

Another important time scale is the *replenishment time* of the matter in the column, $t_\mathrm{r} = M_\mathrm{col}/\dot{M}$, where

$$M_\mathrm{col} = \int_{R_*}^{R_\mathrm{shock}} A_\perp\rho\,\mathrm{d}R \tag{8}$$

is the mass of the accretion column (of all the matter below the shock and above the surface of the star). For a crude estimate, let us assume that $R_\mathrm{shock} - R_* \ll R_*$, and the column itself is in hydrostatic equilibrium. This allows us to replace $\rho\mathrm{d}R = -\mathrm{d}p/g$ (where $g = GM_*/R_*^2$ is the gravity at the NS surface), hence

$$M_\mathrm{col} \simeq (A_\perp p/g)_{R=R_*}. \tag{9}$$

Applying the lower boundary condition $p = B^2/8\pi$ results in a column mass estimate independent of the mass accretion rate. Making

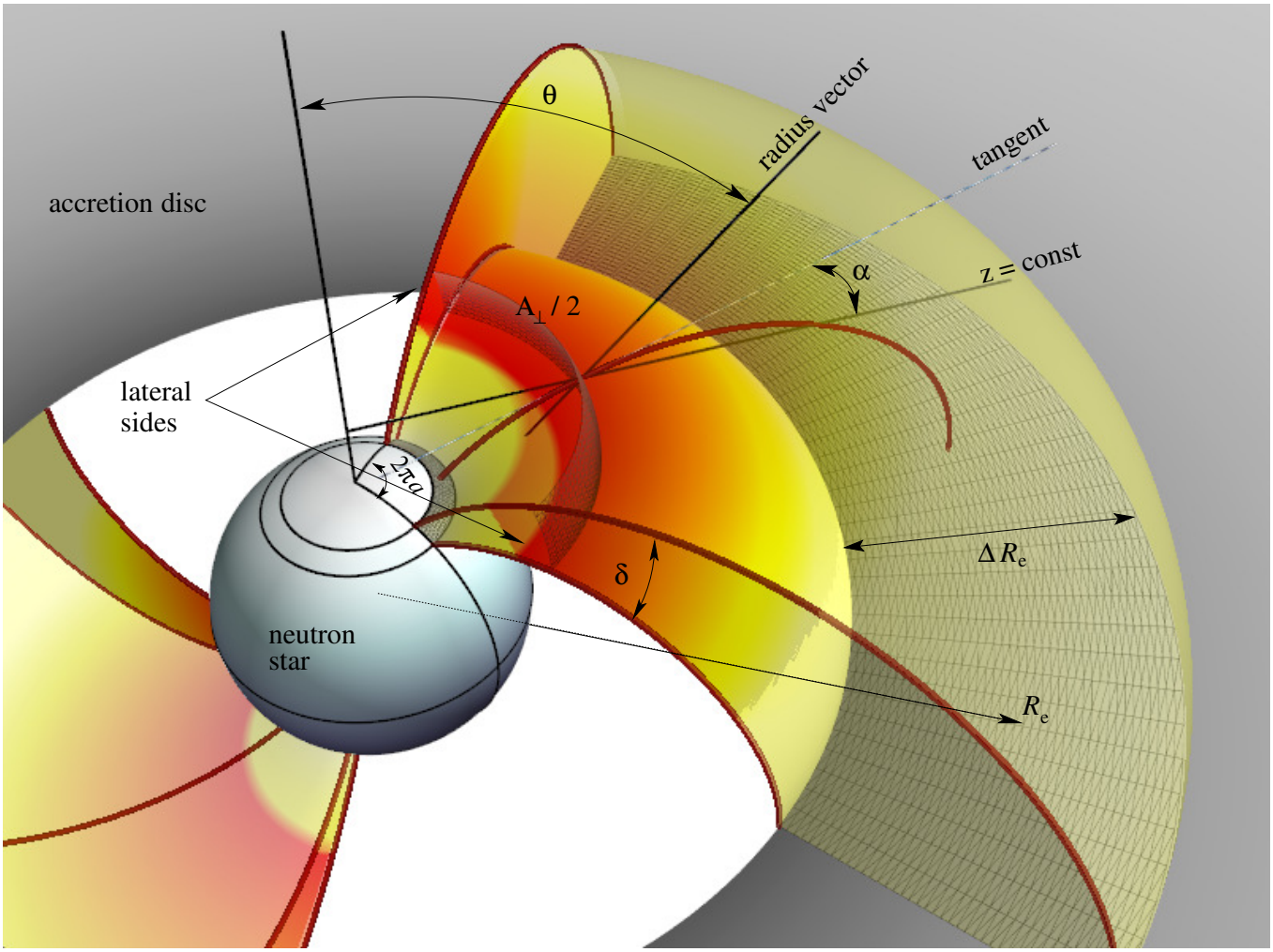

Figure 1. A sketch illustrating the geometry of the problem. Red solid lines are individual magnetic field lines: four on each side restricting the flow and one in the middle. Three cross-sections are shown with hatched shadings, one on the surface, one above the surface, and one in the equatorial plane (outer boundary). The blue dashed line shows a tangent to the field line at the distance where the second cross-section is plotted. We also show radial and z =const lines passing through the same point. Colouring of the sides of the flow shows the pressure (normalised by local magnetic pressure) distribution in the flow according to one of the simulations: yellow corresponds to values about one, red is about 10^{-3}.

all the necessary substitutions, we get an estimate for the replenishment time scale

$$t_\mathrm{r} \simeq \frac{B^2}{8\pi G M}\frac{A_\perp(R_*)R_*^2}{\dot{M}} \simeq 340\left(\frac{B}{10^{12}\,\mathrm{G}}\right)^2\frac{A_\perp(R_*)}{10^{12}\,\mathrm{cm}^2}\left(\frac{R_*}{10\,\mathrm{km}}\right)^2\frac{10^{-8}\,\mathrm{M}_\odot\,\mathrm{yr}^{-1}}{\dot{M}}\,\mathrm{s}, \quad (10)$$

For pulsar-scale magnetic fields and Eddington mass accretion rate $\dot{M} \simeq 10^{-8}\,\mathrm{M}_\odot\,\mathrm{yr}^{-1}$, $A_\perp(R_*) \sim 0.1R_*^2$ (see equation A8), and t_r is of the order of seconds or tens of seconds. The magnetospheres considered in this paper are generally smaller and mostly have $t_\mathrm{r} \sim 0.1$s, depending on the geometric parameters such as a and ΔR_e.

Replenishment time scale is evidently longer than the dynamical time at the surface of the star. It is also likely to exceed the dynamical time scale at the outer edge of the magnetosphere. Using equation (1), it is possible to write down the ratio of the two times as

$$\frac{t_\mathrm{r}}{t_\mathrm{d}(R_\mathrm{e})} = \frac{a\sqrt{2}}{\pi\xi_\mathrm{m}^{7/2}}\frac{\Delta R_\mathrm{e}}{R_*}. \quad (11)$$

As $\xi_\mathrm{m} \sim 1$, $\Delta R_\mathrm{e} \lesssim R_\mathrm{e}$, and $R_* \ll R_\mathrm{e}$, the replenishment time is generally longer than the dynamical time scale at the size of the magnetosphere.

Another crucial time, the time scale for thermal cooling, may be defined as the time required to lose the local internal energy by radiation. In the optically thick parts of the flow, and given $\delta^2 \ll A_\perp$, it may be calculated as the radiation diffusion time scale δ^2/D, where $D = c/3\varkappa\rho$ is the radiation diffusion coefficient. For a stationary flow,

$$t_\mathrm{thermal} \sim \frac{3\varkappa\dot{M}}{cv}\frac{\delta^2}{A_\perp}, \quad (12)$$

where $\varkappa$ is the opacity.

Velocity v varies along the field line from the free-fall velocity above the shock wave to seven times slower below the shock and then essentially to zero near the surface. This makes thermal time

scales extremely long near the basement of the column. To estimate the characteristic maximal cooling times, we can use the analytic solution of BS. The velocity may be obtained by dividing the two equations (32) of BS one over the other and substituting $R = R_*$, that yields for the velocity at the basement of the column

$$v(R_*) \simeq \frac{2\pi\beta_{\rm BS}}{B^2}\frac{GM\dot{M}}{R_* A_\perp(R_*)}\,, \tag{13}$$

where $\beta_{\rm BS}$ is the 'β' parameter used by BS, that has the physical meaning of the fraction of accretion power advected through the surface of the star. For realistic parameter sets, $\beta_{\rm BS}$ varies approximately between 0.1 and 1. Substituting this velocity estimate to (12), we get an expression for the thermal time scale at the bottom of a column

$$\begin{aligned} t_{\rm thermal}(R_*) &\simeq \frac{3B^2}{2\pi\beta_{\rm BS}}\frac{\varkappa}{GMc}R_*\delta^2(R_*) \\ &\simeq 300\frac{1}{\beta_{\rm BS}}\left(\frac{B}{10^{12}{\rm G}}\right)^2\left(\frac{\delta(R_*)}{1\,{\rm km}}\right)^2{\rm s}\,. \end{aligned} \tag{14}$$

2.3 Conservation equations

For a one-dimensional formulation, the basic density quantities (mass density, momentum density, and energy density) need to be integrated in the direction perpendicular to the magnetic field lines. Assuming the physical conditions do not significantly vary across the flux tube, we replace this integration with multiplication by the cross-section $A_\perp$ given by equation (3). Computation involves a finite-volume conservative scheme for the three quantities we treat as conserved: mass, momentum along the field line, and energy, expressed per unit length l along the flux tube (from the computational point of view, it is a single field line)

$$m = \int \rho\,{\rm d}A = \rho A_\perp, \tag{15}$$

$$s = \int \rho v\,{\rm d}A = \rho v A_\perp, \tag{16}$$

$$e = \int \left(u + \rho\,\frac{v^2}{2}\right){\rm d}A = \left(u + \frac{\rho\,v^2}{2}\right)A_\perp. \tag{17}$$

Here, ρ is the volume rest-mass density, v is the velocity along the field line, u is the thermal energy density, consisting of gas $u_{\rm gas}$ and radiation $u_{\rm rad}$ energy densities. We use a kinematic constraint that the matter does not move across the magnetic field lines, and the field lines themselves are not distorted. This justifies the use of a rotating frame and the absence of the kinetic energy of rotation in (17). For each of the three quantities, conservation laws have the general form

$$\frac{\partial q}{\partial t} + \frac{\partial F_q}{\partial l} = S_q, \tag{18}$$

where q refers to a particular quantity (m, s, or e), and F_q and S_q are, respectively, the corresponding flux and the source term. We take the fluxes in the form

$$F_m = \int \rho v\,{\rm d}A = s, \tag{19}$$

$$F_s = \int \left(\rho v^2 + p\right){\rm d}A = sv + A_\perp p, \tag{20}$$

and

$$\begin{aligned} F_e &= \int \left(v\rho\left(\frac{u+p}{\rho} + \frac{v^2}{2}\right) - D\frac{\partial u_{\rm rad}}{\partial l}\right){\rm d}A \\ &= s\left(\frac{u+p}{\rho} + \frac{v^2}{2}\right) - DA_\perp\left(\frac{\partial u_{\rm rad}}{\partial l}\right), \end{aligned} \tag{21}$$

where $D = c/3\varkappa\rho$ is the radiation diffusion coefficient introduced also introduced in Section 2.2. The second term of equation (21) accounts for photon diffusion along the field lines. Thermal pressure p used in equation (21) includes gas and radiation pressure, and is related to the internal energy density as

$$p = \frac{u}{3\,(1-\beta/2)}, \tag{22}$$

and β is defined as the ratio of gas pressure to the total. Pressure ratio may be found by solving numerically (for derivation see Appendix B) the equation for β

$$\frac{\beta}{(1-\beta/2)^{3/4}\,(1-\beta)^{1/4}} = \frac{3}{\sqrt{2}}\frac{k}{\tilde{m}}\left(\frac{c}{\sigma_{\rm SB}}\right)^{1/4}\frac{\rho}{u^{3/4}}\,. \tag{23}$$

Here, k and $\sigma_{\rm SB}$ are, respectively, the Boltzmann and Stefan-Boltzmann constants, and $\tilde{m}$ is the mean particle mass that we set to $\tilde{m} = 0.6\,m_{\rm p}$.

As the accreted matter tends to accumulate at the surface of the star, to reach a stationary state, we need a physically motivated mass sink. At the same time, any mass flows in the direction perpendicular to the direction of the magnetic field are impossible without deforming the field. Hence we add a mass sink that turns on when the local thermal pressure exceeds the pressure of the field $p_{\rm mag} = B^2/8\pi$,

$$S_m = -\frac{m}{A_\perp}\,\Pi\sqrt{\frac{\Gamma_1\max\left(p - p_{\rm mag},\,0\right)}{\rho}}. \tag{24}$$

Here, Π is the perimeter of the flow given by equation (4), and Γ_1 is the effective adiabatic exponent for ideal monatomic gas with a contribution of radiation pressure, see Chandrasekhar (1967, Chapter II, equation 131)

$$\Gamma_1 = \beta + \frac{(4-3\beta)^2\,(\Gamma-1)}{\beta + 12\,(\Gamma-1)\,(1-\beta)}, \tag{25}$$

and $\beta = p_{\rm gas}/p$ is calculated using equation (23), and $\Gamma = 5/3$ as for ideal monatomic gas.

Physically, the loss term given by equation (24) corresponds to all the excess matter escaping the flux tube at about sonic velocity. For the innermost cell of the simulation, it also works as a boundary condition ensuring that, at a mass accretion rate high enough, the energy density at the bottom of the column conforms with the boundary condition used by BS.

The source term for the momentum s is

$$S_s = g_\parallel m + S_m v, \tag{26}$$

where $g_\parallel$ is the force (gravitational, centrifugal, and radiation pressure) per unit mass acting onto the matter in the flow,

$$g_\parallel = -\frac{GM_*}{R^2}\sin(\alpha+\theta)\,(1-\Gamma_{\rm Edd}) + \Omega^2 R\sin\theta\cos\alpha, \tag{27}$$

α is the angle between the tangent to the field line and the direction of the centrifugal force (see Fig. 1), Ω is the rotation frequency of the NS, and

$$\Gamma_{\rm Edd} = \eta_{\rm irr}\frac{L}{L_{\rm Edd}}\frac{1-e^{-\tau}}{\tau} \tag{28}$$

is the correction for radiation pressure (Eddington factor), $\eta_{\rm irr} \lesssim 1$ is

assumed constant, L is the total power lost by the flow as radiation, Eddington luminosity

$$L_{\rm Edd} = \frac{4\pi G M_* c}{\varkappa} \simeq 2\times10^{38}\frac{M_*}{1.4\,{\rm M}_\odot}\,{\rm erg\,s^{-1}}, \quad (29)$$

and τ is the optical depth across the flow in the poloidal direction, estimated as

$$\tau \simeq \tau_\theta = \varkappa\rho\delta = \varkappa\frac{\delta}{A_\perp}m\,. \quad (30)$$

The last term in (26) accounts for the momentum lost with the expelled mass.

In this work, we use the opacity of $\varkappa = 0.35\,{\rm cm^2\,g^{-1}}$, approximately equal to the Thomson scattering opacity for Solar metallicity in the assumption of complete ionisation. We neglect the influence of the magnetic field upon the scattering cross-section, that could be an important factor for large magnetic fields (Basko & Sunyaev 1975; Arons et al. 1987; Becker & Wolff 2007).

Here, we consider three different contributions to energy sources and sinks: work done by the external forces, energy loss due to radiation, and the energy lost with the mass loss

$$S_e = g_\parallel s - \frac{1-e^{-\tau_{\rm eff}}}{\xi_{\rm rad}\tau_{\rm eff}+1}\,c\,\Pi u_{\rm rad} + S_m\frac{e+pA_\perp}{m}, \quad (31)$$

where $\xi_{\rm rad} \sim 1$ is a dimensionless factor taking into account the transverse structure of the flow. When energy is released in the middle of the accretion column, $\xi_{\rm rad} = 3/2$. Assuming the energy sources uniformly distributed over the cross-section would instead lead to $\xi_{\rm rad} = 3/4$. Both possibilities are mentioned in BS, and the first one used for the calculations. We also use $\xi_{\rm rad} = 3/2$ everywhere in this paper. The $1-e^{-\tau_{\rm eff}}$ factor in the second term of equation (31) allows us to extend the results to the case of low optical depths, where the radiation losses are volumetric rather than areal. We use the effective optical depth defined as

$$\tau_{\rm eff} = \varkappa\, m\, \delta_{\rm eff}/A_\perp, \quad (32)$$

where

$$\delta_{\rm eff}^{-1} = \delta^{-1} + 2\delta/A_\perp. \quad (33)$$

For the models where emission from the lateral sides is ignored, $\delta_{\rm eff} = \delta$, $\tau_{\rm eff} = \tau_\theta$, and perimeter $\Pi = 2A_\perp/\delta$. equation (32) reproduces the optical depth in the two extreme cases, when $A_\perp/2\delta$ is either much smaller or much larger than δ. The last term in (31) corresponds to the matter lost from the column when the mass sink is on. As work should be done to expel matter, there is a contribution from pressure in the term. In one of the models, we turn the pressure contribution off in this term to facilitate the comparison with the results of BS.

The resulting system of three differential equations takes the form

$$\frac{\partial m}{\partial t} + \frac{\partial s}{\partial l} = S_m, \quad (34)$$

$$\frac{\partial s}{\partial t} + \frac{\partial F_s}{\partial l} = S_s, \quad (35)$$

and

$$\frac{\partial e}{\partial t} + \frac{\partial F_e}{\partial l} = S_e, \quad (36)$$

where the densities, fluxes, and sources are given by equations (15-17), (19-21), (24), (26), and (31). The independent variable l is related to the radial coordinate by equation (5). The cross-section of the flow used by the expressions for fluxes and sources is calculated according to equation (3).

Solving the above system of equations yields physical parameters as functions of time t and spherical radius R. The bolometric luminosity is calculated by integration of the second term of (31) along the flux tube as

$$L = \int Q^-\Pi\,{\rm d}l = \int \frac{1-e^{-\tau_{\rm eff}}}{\xi_{\rm rad}\tau_{\rm eff}+1}\,c\,\Pi\,u_{\rm rad}\,{\rm d}l, \quad (37)$$

where perimeter Π is given by equation (4), $\tau_{\rm eff}$ by equation (32), and

$$Q^- = \frac{1-e^{-\tau_{\rm eff}}}{\xi_{\rm rad}\tau_{\rm eff}+1}\,c\,u_{\rm rad} \quad (38)$$

is the radiation flux leaving the surface of the column. The integral in equation (37) taken over the whole simulation domain will be denoted $L_{\rm tot}$, and below the shock $L_{\rm X}$, for consistency with BS.

2.4 Numerical method

System of equations (34–36) is solved using HLLE (Harten – Lax – van Leer – Einfeldt) Riemann solver (Harten et al. 1983; Einfeldt 1988). Signal velocities used in this solver are calculated according to the 'hybrid' method of Toro et al. (1994), with the effective adiabate exponent set to $\Gamma_{\rm eff} = 5/3$. Hence, the adopted maximal signal velocity is slightly larger than the accurate value predicted by equation (25). This adds diffusivity to the solution but increases its stability in the case of rapid variations of Γ_1.

The problem is challenging for numerical consideration, as density and velocity vary by many orders of magnitude. For the configurations considered in this paper, Mach number $\mathcal{M}$ changes from tens above the shock front to about 10^{-5} near the surface of the NS. While existence of a shock front is not a problem for an HLLE solver, low Mach values cause the so-called stiffness problem (Keshtiban et al. 2003). In eliminating the problem, we find the pre-conditioning technique introduced by Turkel (1999) sufficient for our needs. For Mach numbers smaller than 1, signal velocities used by the Riemann solver are multiplied by $\mathcal{M}$, that efficiently removes the spurious flux biases in the low-velocity regions.

The purpose of a Riemann solver is conversion between the fluxes calculated at the midpoints of the cells and the fluxes at the cell boundaries. The energy flux given by equation (21) contains a photon diffusion term that is immediately calculable at the cell boundaries as

$$-DA_\perp\frac{\partial u_{\rm rad}}{\partial l} \simeq \frac{cA_\perp}{3}\frac{u_{{\rm rad},\,i+1}-u_{{\rm rad},\,i}}{\tau_i} \quad (39)$$

where $\tau_i = \varkappa\int_{l_i}^{l_{i+1}}\rho\,{\rm d}l \simeq (\rho_i+\rho_{i+1})(l_{i+1}-l_i)/2$ is the optical depth between the centers of the i-th and the $i+1$-th cells. The standard HLLE solver is used for the rest of the flux terms.

2.5 Boundary and initial conditions

As the inner boundary conditions, we use zero velocity (hence $F_m(R_*) = s(R_*) = 0$) and zero thermal energy flux (that implies $F_e(R = R_*) = 0$). In the lower parts of the column, mass and energy accumulate until the pressure of the flow exceeds the local magnetic field pressure, and the mass-loss term (24) turns on. If the mass loss starts at the bottom, the boundary condition used by BS is reproduced.

At the outer boundary, we fix the mass flux F_m (and thus momentum density $s = F_m$) to $-\dot{M}$. The material entering at the outer boundary is assumed to have the velocity of $v(R_{\rm e}) = -\sqrt{GM_*/R_{\rm e}}$.

Knowing the mass flux and the velocity at the outer boundary allows one to calculate the value of density ρ. Thermal energy density u at the outer boundary was chosen equal to the magnetic energy density at this distance. As the transverse optical depth of the flow above the shock is usually small, most of this internal energy is radiated away above the shock wave. Hence, the flow is always gravitationally bound.

The total energy radiated by a steady-state flow is

$$L_{\rm tot} = \frac{GM_*\dot{M}}{R_*} - \frac{GM_*\dot{M}}{2R_{\rm e}} + L_{\rm out} - L_{\rm vent}\,, \tag{40}$$

where

$$L_{\rm out} = \dot{M}\,\left.\frac{u+p}{\rho}\right|_{R_{\rm e}} \tag{41}$$

is the heat entering through the outer boundary per unit time, and $L_{\rm vent}$ is the energy loss associated with the mass loss from the column (third term of equation 31 integrated along the field line). The quantities $\dot{M}$, ρ, and u in equation (41) are set by the boundary conditions, and p may be derived from ρ and u using the formulae of Appendix B. Usually the first term of equation (40),

$$L_{\rm acc} = \frac{GM\dot{M}}{R_*}, \tag{42}$$

dominates, and the thermal contribution of the outer boundary condition is small. However, for low accretion rates, the latter can significantly alter the total luminosity of the flow. On the other hand, the measured steady-state luminosity may be (and usually is) smaller than $L_{\rm acc}$ because of the adopted mass and the energy sink represented by $L_{\rm vent}$.

Initial conditions are approximately constant mass density and sub-virial negative velocity approaching zero at the inner boundary. We choose the total initial mass equal to 10 per cent of the equilibrium column mass defined as (equation 9), that allows the flow to approach a quasi-stationary regime in several replenishment times (equation 10). The relatively slow approach to equilibrium (see section 3) is probably related to very long thermal time scale at the bottom of the column (equation 14).

2.6 Time steps

Ignoring the effects of radiation losses, we can estimate the time step required for stability as

$$\Delta t_{\rm CFL} \simeq C_{\rm CFL}\left(\frac{\Delta l}{|v|+c_{\rm s}}\right)_{\rm min}, \tag{43}$$

where $C_{\rm CFL} \lesssim 1$ is the Courant-Friedrichs-Levy multiplier (Courant et al. 1967). However, local thermal radiation loss and diffusion time scales sometimes become smaller than (43), and this requires refinement of the time step. Thermal cooling time scale may be estimated using the radiation loss term in equation (31), as

$$\Delta t_{\rm thermal} \simeq \frac{u_{\rm rad}A_\perp}{\Pi Q^-} = \frac{\delta_{\rm eff}}{2c}\,\frac{1+\xi_{\rm rad}\tau_{\rm eff}}{1-e^{-\tau_{\rm eff}}}\,. \tag{44}$$

For a stationary flow with a large optical depth, this may be further simplified to

$$\Delta t_{\rm thermal} \simeq \frac{\xi_{\rm rad}}{2c}\,\frac{\varkappa\dot{M}\,\delta_{\rm eff}^2}{A_\perp v}. \tag{45}$$

If the radiation from the lateral sides is ignored, this expression reduces (up to a factor of 4) to equation (12).

The upper limit for the diffusion equation time step is estimated as (see, for example, the first appendix of Tikhonov & Samarskii 2013):

$$\Delta t_{\rm diff} \simeq C_{\rm diff}\left(\frac{\Delta l^2}{D}\right)_{\rm min}, \tag{46}$$

where $C_{\rm diff} \le 0.5$ is a dimensionless factor. Overall stability of the numerical solution requires a time step smaller than the smallest of all the three, hence we used the smallest of the three lower limits

$$\Delta t = \min\left(\min\Delta t_{\rm CFL},\ \min\Delta t_{\rm thermal},\ \min\Delta t_{\rm diff}\right), \tag{47}$$

where the three time steps are given by equations (43), (44), and (46).

3 RESULTS

3.1 General picture and shock formation

In Table 1, we summarize the parameters of the models. The models have different mass accretion rates, magnetic moments, and azimuthal extents of the flow. The mass of the NS is everywhere set to $1.4\,{\rm M}_\odot$, and its radius to $4.86\,GM_*/c^2 \simeq 10\,$km. For most of the models, we adopt the relative width of the flow at the outer boundary $\Delta R_{\rm e}/R_{\rm e} = 0.25$. The effective size of the magnetosphere was calculated as $R_{\rm e} = \xi_{\rm m}R_{\rm A}$, where $\xi_{\rm m}$ is set to 0.5, and $R_{\rm A}$ according is Alfven radius given by equation (1). For most of the simulations, the size of the magnetosphere is about $14R_*$. Coordinate mesh is approximately logarithmic in l, with the total number of 9600 radial points for the fiducial model. This gives a resolution of about $\Delta l \sim 3\times10^{-4}R_*$ near the surface of the NS, and $\Delta l \sim 4\times10^{-3}R_*$ close to the outer edge. Most simulations are run for tens of replenishment times, ensuring that mass loss starts well before the end of the simulation. Output is made each $0.01t_{\rm r}$. For model H, the output is intentionally made ten times more often to track the dynamical-time-scale variability.

Table 1 also contains the quantity $\beta_{\rm BS}$, that is the combination of global parameters (geometry, magnetic moment, and mass accretion rate) that determines the fraction of the accretion luminosity advected towards the NS surface in the solution of BS. To calculate this parameter, we used the expressions of section 4.4 of BS. Detailed comparison with the analytic solution will be done later in section 3.3.

From the beginning, the flow, initially practically static (velocities much smaller than Keplerian by absolute values), starts falling along the field lines. The infall leads to adiabatic heating and subsequently to the formation of a shock near the bottom of the simulation domain. The shock moves upward, approaching the equilibrium position even before the beginning of the mass loss. In the steady state, the flow in the column is heated by adiabatic compression, while the excess thermal energy is radiated away. Energy release and radiation loss evolve towards the equilibrium on the time scale close to replenishment time (equation 10) or the thermal time at the bottom of the column (equation 14).

In all the simulations, the shock oscillates before reaching the steady state. The oscillations are damped, though it is difficult to decide if the damping is physical or numerical. We discuss these oscillations in more detail in section 3.6. In Fig. 2, we show the development of the shock wave on the time-radius plots for velocity and thermal energy density for model N. In the velocity plot, the shock wave is clearly seen as the boundary between the almost static region closer to the surface of the star (column) and the nearly free-falling region above.

In Table 2, we give the position of the shock and different characteristic luminosities emitted by the flow after it reaches a steady

Table 1. Parameters of the simulations. First column gives the identifier of the model used throughout the paper. Subsequent columns are: mass accretion rate normalised by the Eddington value, magnetic moment, azimuthal fraction a occupied by the flow, radius of the magnetosphere, normalised cross-section and latitudinal thickness of the flow near the surface of the star, replenishment time (equation 10), duration of the simulation, Basko-Sunyaev's advection parameter $\beta_{\rm BS}$, and essential comments about the particular simulation. All the models with $a = 1$ have no cooling from the lateral sides.

ID	$\frac{\dot{M}_{\rm out}c^2}{L_{\rm Edd}}$	μ_{30}, 10^{30} g cm^3	a	$R_{\rm e}/R_*$	$A_\perp(R_*)/R_*^2$	$\delta(R_*)/R_*$	$t_{\rm r}$, s	$t_{\rm max}$, s	$\beta_{\rm BS}$	comment
F	10	0.1	0.25	13.95	2.89×10^{-2}	0.0344	0.11	1	0.43	fiducial
L	10	0.1	0.25	13.95	2.89×10^{-2}	0.0344	0.11	1.4	0.43	2X coarser resolution
F2	10	0.1	0.25	13.95	2.89×10^{-2}	0.0344	0.11	1	0.43	2X finer resolution
ND	10	0.1	0.25	13.95	2.89×10^{-2}	0.0344	0.11	2	0.43	no radial photon diffusion
B	10	0.1	0.25	13.95	2.89×10^{-2}	0.0344	0.11	2	0.43	no radial photon diffusion; no radiation losses from lateral sides
M1	1	0.03	0.25	13.53	2.985×10^{-2}	0.0350	0.10	1.1	0.10	
M3	3	0.05	0.25	13.24	3.05×10^{-2}	0.0353	0.10	0.6	0.22	
M30	30	0.2	0.25	14.19	2.66×10^{-2}	0.0330	0.14	2	0.64	
M100	100	0.3	0.25	13.53	2.99×10^{-2}	0.0345	0.10	2	0.81	
W	10	0.1	1	13.95	0.116	0.0344	0.0269	2	0.45	no cooling from the lateral sides
N	10	0.1	0.05	13.95	5.79×10^{-3}	0.0344	0.022	0.38	0.73	
N2	10	0.1	0.05	13.95	5.79×10^{-3}	0.0344	0.022	0.38	0.73	no cooling from the lateral sides
R	10	0.1	0.25	13.95	2.89×10^{-2}	0.0344	0.11	1.9	0.43	$\Omega = 0.9\Omega_{\rm K}(R_{\rm e})$
I	10	0.1	0.25	13.95	2.89×10^{-2}	0.0344	0.11	0.9	0.43	irradiation $\eta_{\rm irr} = 0.5$
WI	10	0.1	1	13.95	0.116	0.0344	0.0269	1.8	0.45	same as W but $\eta_{\rm irr} = 0.5$
WI1	10	0.1	1	13.95	0.116	0.0344	0.0269	1.9	0.45	same as W but $\eta_{\rm irr} = 1$
RI	10	0.1	0.25	13.95	2.89×10^{-2}	0.0344	0.11	0.8	0.43	$\Omega = 0.9\Omega_{\rm K}(R_{\rm e})$, $\eta = 0.5$
H	10	1	0.25	52.0	7.61×10^{-3}	0.0175	2.9	1.4	0.417	
M100W2x	100	0.3	1.0	23.7	0.118	0.0488	0.4	3.5	0.72	$\Delta R_{\rm e}/R_{\rm e} = 0.5$, $\xi_{\rm m} = 1$, 2X coarser resolution
M100W3	100	0.3	1.0	13.53	0.143	0.0419	0.50	2	0.63	$\Delta R_{\rm e}/R_{\rm e} = 0.3$
M100W4	100	0.3	1.0	13.53	0.119	0.0350	0.42	2	0.60	
M100W5	100	0.3	1.0	13.53	0.0955	0.0280	0.33	2	0.56	$\Delta R_{\rm e}/R_{\rm e} = 0.2$
M100W10	100	0.3	1.0	13.53	0.0478	0.0140	0.17	3	0.43	$\Delta R_{\rm e}/R_{\rm e} = 0.1$
M100W20	100	0.3	1.0	13.53	0.0239	0.00700	0.08	1.4	0.308	$\Delta R_{\rm e}/R_{\rm e} = 0.05$
M100W50	100	0.3	1.0	13.53	0.00955	0.00280	0.033	0.6	0.178	$\Delta R_{\rm e}/R_{\rm e} = 0.02$

state. The luminosity of the flow is integrated using equation (37) over the whole simulation domain ($L_{\rm tot}$) and below the shock wave ($L_{\rm X}$). $L_{\rm out}$ is the thermal power entering from the outer border (see equation 41). The last column in Table 2 gives the fraction of the luminosity that is not radiated by the accretion column but rather lost with the mass. In our setup, its role is the same as of the advected power fraction in BS. For most of the models, $1 - L_{\rm X}/L_{\rm acc} \simeq \beta_{\rm BS}$, and the deviations are mostly related to the emission from the lateral sides or to the heat flux at the outer boundary (as in `M3` where the total luminosity is larger than $L_{\rm acc}$).

3.2 Mass leakage from the column

After the position of the shock stabilises, mass starts being lost from the column. The higher the position of the shock front, the higher the place where thermal pressure starts exceeding magnetic pressure. In general, the region where the mass leaks from the column (that we will hereafter refer to as the *vent*) is formed above the surface of the star, sometimes at a height comparable to the radius of the NS.

In Table 3, we give the radial coordinates at which the vents first appear in the models where the vent first appears at a considerable altitude. The initial vent position depends not only on the accretion rate but also on the geometry of the flow. In particular, for model `N2` (Fig. 2), the critical energy density is reached at about $2R_*$, though the mass accretion rate is the same as in model `F`, where the vent appears very close to the surface. In most of the cases (with the exception of models `N2`, `M100` and `M100W2x`, considered in more detail later in section 3.4) when the vent is formed well above the surface, it gradually drifts downwards and eventually reaches the surface of the star.

There are several parameters that define the geometry of an accretion column. Small radiating perimeter Π (as in models `N` and `N2`) decreases the radiating surface, thereby trapping more heat inside the column. This leads to a higher shock and a higher initial vent, especially in `N2` where the radiation losses from the lateral sides of the column are ignored. Decreasing the latitudinal size of the column (by decreasing $\Delta R_{\rm e}$), on the other hand, facilitates cooling of the column by decreasing the average optical depth, and the mass leakage starts closer to the surface.

Very tall columns like that in `N2` may have several vents at different heights in the steady-state regime. For `M100`, where no stationary shock wave develops, mass loss occurs over a broad range of heights, approximately from 1 to $2.5-3\,R_*$. We will discuss the behaviour of these models in more detail in section 3.4. To sum up, same factors (accretion rate and flow geometry) affect the height of the column (the shock position) and the initial vent position.

In Fig. 4, we show the evolution of the mass flux during the initial 0.05 s (about half of the replenishment time) for three different

Table 2. Parameters of the column measured for the last 10 per cent of the simulation time for different models. Luminosities $L_{\rm tot}$ and $L_{\rm X}$ are calculated by integrating the radiation flux over the whole simulation and below the shock, respectively. 'Predicted' shock position and luminosity are estimated in the framework of the analytic model by BS. Luminosities $L_{\rm acc}$, $L_{\rm tot}$, $L_{\rm X}$, and $L_{\rm out}$ are defined in sections 2.3 and 2.5.

ID	$R_{\rm shock}/R_*$		$L_{\rm tot}/L_{\rm Edd}$	$L_{\rm acc}/L_{\rm Edd}$	$L_{\rm X}/L_{\rm Edd}$		$L_{\rm out}/L_{\rm Edd}$	$1-\frac{L_{\rm X}}{L_{\rm acc}}$
	measured	predicted			measured	predicted		
F	3.238±0.005	3.58	1.44	2.06	1.16	1.17	0.38	0.44
L	3.238±0.009	3.58	1.44	2.06	1.16	1.17	0.38	0.44
F2	3.237±0.002	3.58	1.42	2.06	1.17	1.17	0.38	0.43
ND	3.260±0.005	3.58	1.33	2.06	1.18	1.17	0.38	0.43
B	3.567±0.005	3.58	1.27	2.06	1.12	1.17	0.38	0.46
M1	1.3724±0.0019	1.42	0.201	0.205	0.180	0.184	0.21	0.12
M3	1.837±0.004	1.99	0.70	0.53	0.66	0.48	0.21	-0.24
M30	6.506±0.010	7.39	2.70	6.15	2.16	1.16	0.72	0.65
M100	–	17.87	3.67	20.5	–	3.89	2.3	–
W	1.980±0.003	1.97	2.87	2.06	1.63	1.65	1.30	0.21
N	4.982±0.007	8.47	0.81	2.06	0.72	0.55	0.13	0.65
N2	8.447±0.04	8.47	0.57	2.06	0.51	0.55	0.13	0.75
R	3.137±0.004	3.58	1.25	2.06	1.09	1.17	0.38	0.47
I	3.256±0.005	3.58	1.34	2.06	1.19	1.17	0.38	0.42
WI	1.962±0.003	1.97	2.8	2.06	1.55	1.65	1.29	0.25
WI1	1.98±0.04	1.97	2.05	2.06	1.64	1.65	1.33	0.20
RI	3.215±0.005	3.58	1.31	2.06	1.16	1.17	0.38	0.44
H	3.786±0.004	4.40	1.31	2.05	1.26	1.20	0.47	0.39
M100W2x	10.73±0.04	12.1	6.35	20.5	5.59	5.74	2.19	0.73
M100W3	12.450±0.010	8.44	10.8	20.5	9.9	7.6	6.5	0.52
M100W4	8.869±0.016	7.27	12.8	20.5	9.2	8.3	6.1	0.55
M100W5	6.485±0.009	6.09	12.8	20.5	9.1	9.2	5.3	0.56
M100W10	3.733±0.005	3.71	13.7	20.5	11.5	11.7	3.15	0.44
M100W20	2.458±0.003	2.47	15.2	20.5	13.8	14.2	1.97	0.33
M100W50	1.656±0.002	1.66	17.3	20.5	16.1	16.7	1.23	0.21

Table 3. The initial position of the vent and the time of its opening for different models.

ID	$R_{\rm vent}/R_*$	t_0, ms
F	1.00 ± 0.0003	207.52 ± 0.04
F2	1.00 ± 0.0003	207.86 ± 0.04
B	1.0 ± 0.0003	233.80 ± 0.04
N	1.0538 ± 0.0003	79.10 ± 0.08
N2	1.9096 ± 0.0005	96.18 ± 0.08
M30	1.0381 ± 0.0003	466.0 ± 0.5
M100	11.263 ± 0.002	6.20 ± 0.04
M100W2x	1.5430 ± 0.0010	813.3 ± 0.4
M100W3	1.0808 ± 0.0002	1909 ± 2
M100W4	1.0229 ± 0.0003	1380.0 ± 1.4
M100W5	1.0122 ± 0.0003	946 ± 11
M100W10	1.0003 ± 0.0003	344.1 ± 0.6
M100W20	1.0 ± 0.0003	141.1 ± 0.3
M100W50	1.0 ± 0.0003	81.78 ± 0.11

models. While above the shock, the mass accretion rate $s = \rho v A_\perp$ is very stable and close to $\dot{M}$, matter inside the column is, for most of the models, involved in a cyclic motion with the velocity amplitude exceeding the mean velocity value. Initial shock oscillations leave entropy traces in the flow, that are best visible in the diagram for `M100`. In `N2` and in `M100`, the oscillations do not show any damping, and the position of the vent neither stabilises nor approaches the surface of the star. In `M100W2x`, the oscillations are damped significantly, and the flow structure stabilises, with the position of the vent at a height of about $0.2R_*$ above the NS surface. The damping may be a consequence of the lower resolution of this model.

3.3 Structure of the flow and comparison with the analytical model

The shock front position is easy to find as the position of the velocity derivative maximum. In Fig. 5, we show the position of the shock front as a function of time and below-the-shock luminosity $L_{\rm X}$ for the fiducial model `F`. In simulation `F`, mass starts to leak out at $t \sim 0.2$ s, which is visible in the left panel of Fig. 5 as a break in the shock front motion law.

We compare the position of the shock with the prediction of equation 34 of BS

$$\eta\gamma^{1/4}\xi_{\rm s}^{n/4+1/8} = 1 + {\rm e}^{\gamma\xi_{\rm s}}\left[\xi_{\rm s}{\rm E}_2(\gamma) - {\rm E}_2(\gamma\xi_{\rm s})\right], \tag{48}$$

that implicitly defines the radial coordinate of the shock $\xi_{\rm s} = R_{\rm shock}/R_*$. Here, n is a dimensionless parameter describing the curvature of the field lines (for dipolar geometry, $n = 3$), and

$${\rm E}_k(x) = \int_1^{+\infty} t^{-k}{\rm e}^{-tx}{\rm d}t \tag{49}$$

is the exponential integral of order k. Dimensionless coefficients γ and η in equation (48) are

$$\begin{aligned}\gamma &= \frac{c\,R_*}{\varkappa\delta^2(R_*)}\frac{A_\perp(R_*)}{\dot{M}}\frac{3}{2\xi_{\rm rad}}\\ &\simeq 0.387\,\frac{A_\perp(R_*)}{\delta^2(R_*)}\frac{L_{\rm Edd}}{\dot{M}_{\rm out}c^2}\frac{R_*c^2}{4.86GM_*}\frac{3}{2\xi_{\rm rad}}\end{aligned} \tag{50}$$

and

$$\begin{aligned}\eta &= \left(\frac{8\varkappa}{21c}\frac{3p_{\rm mag}(R_*)\,\delta^2(R_*)}{\sqrt{2GM_*R_*}}\frac{2\xi_{\rm rad}}{3}\right)^{1/4}\\ &\simeq 12.57\left(\frac{B}{10^{12}{\rm G}}\right)^{1/2}\left(\frac{\delta(R_*)}{0.03R_*}\right)^{1/2}\left(\frac{R_*c^2}{4.86GM_*}\right)^{3/8}\left(\frac{M}{1.4\,{\rm M}_\odot}\right)^{1/4}.\end{aligned}$$

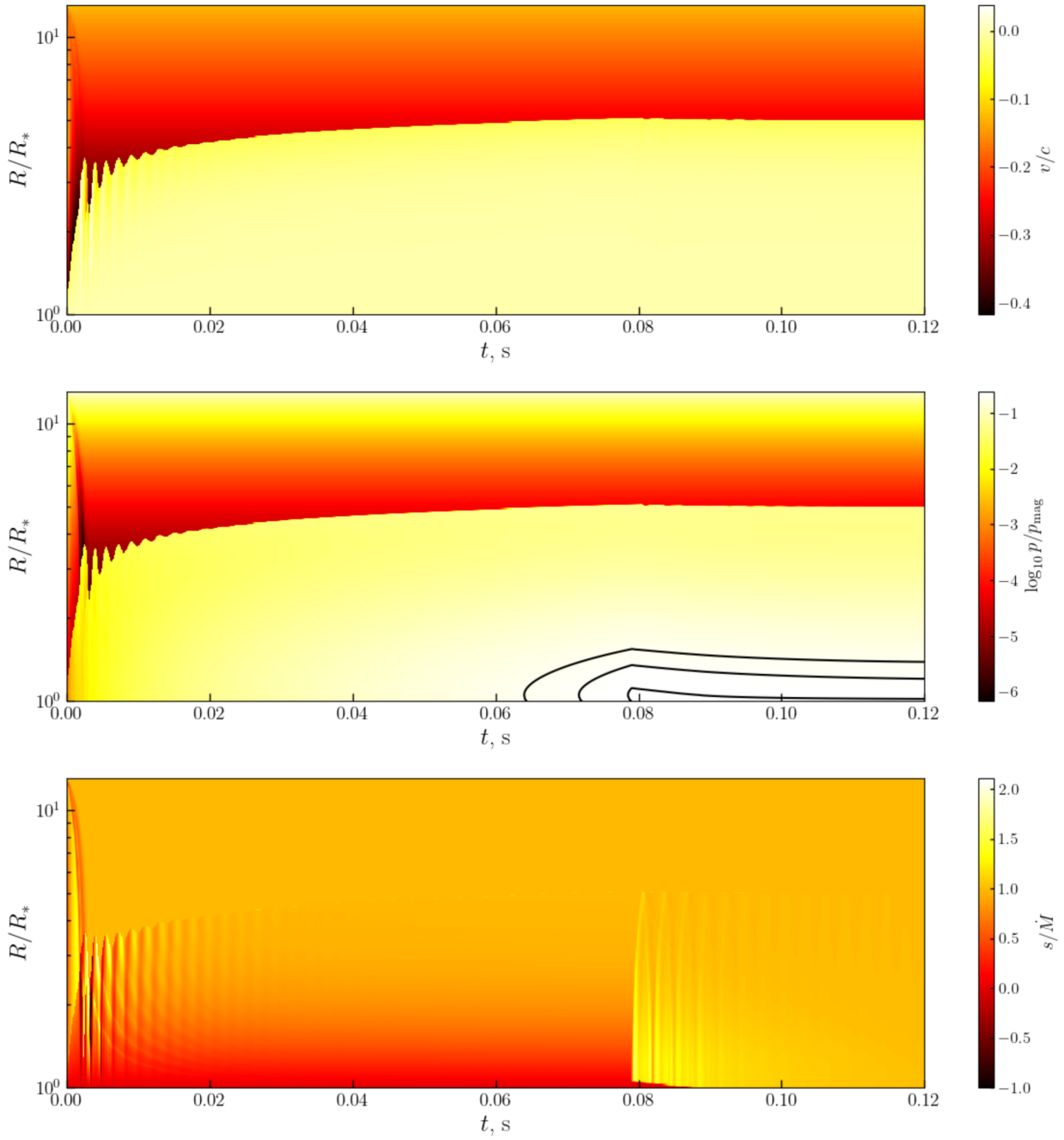

Figure 2. Time-radius diagrams for velocity (upper panel), thermal pressure (middle panel; the logarithm of the quantity in $p_{\rm mag}$ units is shown), and mass flux s (lower panel; the quantity is normalised by the mass accretion rate at the outer boundary) for the first 0.12 s of simulation `N`. Black contours in the middle panel correspond to pressure equal to 80, 90, and 99 per cent of the magnetic field pressure.

(51)

In comparison with the original expressions of BS, equations (50) and (51) contain an extra factor of $2\xi_{\rm rad}/3$, resulting from the radiation diffusion across the flow, parameterised by the coefficient $\xi_{\rm rad}$. Here, we set $\xi_{\rm rad} = 3/2$, that corresponds to all the energy released in the middle of the column.

Position of the shock $\xi_{\rm s}$ and the two parameters γ and η may be used to find the advection parameter as

$$\beta_{\rm BS} = 1 - \gamma e^{\gamma} \left[{\rm E}_1(\gamma) - {\rm E}_1(\gamma \xi_{\rm s}) \right] . \quad (52)$$

The luminosity of the column itself is then equal to $(1 - \beta_{\rm BS})\, L_{\rm acc}$. With few exceptions, we find this estimate to work well for our simulations after they enter the steady-state regime (see section 3.1 and Tables 1 and 2).

In Table 2, we give the shock positions predicted by BS as well as the simulation results. For `B` and several other models, the prediction is pretty accurate (about 0.4 per cent for `B`). Most of the difference between predicted and calculated quantities in Table 2 comes from the radiation losses from the lateral sides of the column. Also, the higher

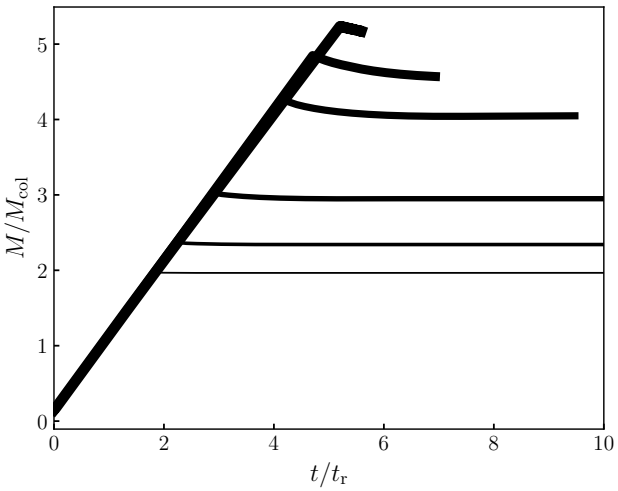

Figure 3. Total mass (in the estimated column mass units, see equation 9) as a function of time (replenishment time units, equation 10) for models `M100W3-50`, from the thickest to the thinnest curve.

the shock position, the less accurate is the analytic approximation, as the latter does not account for the real dipole geometry. The shock position is not very sensitive to the effects of photon diffusion (compare `F` and `ND`). Other physical effects also affect only slightly the shock position, as we demonstrate later in section 3.5.

Our fiducial model uses physical assumptions different from that of the analytic model by BS. Apart from time dependence, we use dipole geometry, different set of boundary conditions, and allow for photon diffusion along magnetic field lines. In model `B`, photon diffusion is turned off, and the contribution of the lateral sides of the column to radiation losses is ignored. This conforms well to the assumptions of BS, and allows straightforward comparison to the analytic solution. Quite expectedly, the shock position in `B` is very close to the predicted value.

The effect of changing geometry, as well as consistency with BS, is illustrated by Fig. 6, where we show six models `M100W3-50`, differing only in the width of the penetration zone, and an additional model `M100W2x`, having similar geometry but a larger magnetosphere. For a fixed mass accretion rate, smaller δ means higher surface-to-volume ratio, more efficient cooling and thus lower shock and vent positions. For small advection parameters $\beta_{\rm BS} \lesssim 0.6$, there is good agreement between our simulations the analytic results, while the last three points deviate from the analytic model considerably.

While the position of the shock is generally well predicted by the analytical solution, the differences in the detailed column structure are more pronounced (see Figs 7 and 8). In Fig. 7, we compare time-averaged properties of the simulated flow with the analytic solution. Certain differences arise from the boundary conditions near the surface of the NS. While the analytic model requires a non-zero velocity at $R = R_*$, our model allows the matter to seep out at a zero radial velocity. Existence of such a sink creates a velocity discontinuity near the surface, above which the flow moves at a speed even higher than predicted by the analytic model.

Another difference between our results and analytic predictions is in the contribution of the gas pressure. While $p_{\rm gas}$ is still much smaller than $p_{\rm rad}$ everywhere below the shock, the value of $\beta = p_{\rm gas}/p$ differs from the analytic model by up to a factor of 2 near the surface.

3.4 Breakdown at large accretion rates

For some combinations of parameters, the steady-state solution is physically inconsistent. This is generally the case for the parameter values predicting a very tall column, like those of our models `N2` (see Fig. 8), `M100`, and `M1002x`. For `M100`, the predicted height of the column is larger than the size of the magnetosphere, hence we do not expect any agreement in the structure of the column.

The analytic solution for the parameters corresponding to `N2` is self-inconsistent, as it predicts radiation pressure higher than magnetic pressure at a finite height above the NS surface. Because of our assumptions about the mass loss from the column, pressure in the simulation practically never exceeds the pressure of the magnetic field (see Fig. 8). Instead, the column leaks over a broad range of heights, up to about $3\,R_*$. However, the predicted height of the column agrees well with the results of our simulation, and the structure of the solution is similar. A similar picture is seen for `M100`, where no stationary shock is developed, and the matter is lost from a large span of radial coordinates. In `M100W2x`, the positions of both the shock and the vent stabilise with time, but the vent is located well above the surface.

A sufficient condition for the analytic solution to become self-inconsistent is a shallow enough radial dependence of $u(R)$ near $R = R_*$. If for radiation-pressure-dominated gas

$$\left.\frac{{\rm d}\ln p}{{\rm d}\ln R}\right|_{R=R_*} > -6, \tag{53}$$

the boundary condition $p = p_{\rm mag}$ at the surface of the star implies $p > p_{\rm mag}$ somewhere above the surface. One can check that for the solution given by equation (32) of BS, this is equivalent to $\beta_{\rm BS} > 2/3$.

As $\beta_{\rm BS}$ has the physical meaning of the power fraction trapped within the accretion column, large values of $\beta_{\rm BS}$ mean inefficient radiation losses from its surface. Inefficient cooling of the column not only increases its supply of thermal energy, but also leads to a shallow energy density profile, and, as a consequence, overheating of the column at a finite height. Indeed, in an advection-dominated column (in the limit $\beta_{\rm BS} \to 1$), the power advected vertically at some radius R is

$$uvA_\perp \simeq \frac{GM_*\dot{M}}{R} = \frac{GM_*}{R}A_\perp\rho v, \tag{54}$$

that implies virial scaling $u \propto \frac{GM}{R}\rho$. At the same time, for radiation-pressure-dominated matter, $u \propto \rho^{4/3}$. Radiation energy density should thus depend on radius as $u \propto R^{-4}$, while $p_{\rm mag} \propto R^{-6}$.

One can see from Tables 1 and 2 that this condition for $\beta_{\rm BS}$ may be used as an applicability criterion for the analytic model: all the models with $\beta_{\rm BS} < 2/3$ are in good agreement with the analytic model, while large values of $\beta_{\rm BS}$ lead to column overheating and mass loss from the column at a finite height above the NS surface. Even then, as long as the position of the shock is much lower than the size of the magnetosphere, the analytic solution by BS gives a good approximation for the position of the shock and the structure of the column.

3.5 Contribution of different physical and numerical effects

3.5.1 Numerical resolution and photon diffusion

In Fig. 9, we show how the distribution of effective temperature (calculated using the local radiation flux as $Q^- = \sigma_{\rm SB}T_{\rm eff}^4$) depends on spatial resolution: models `F` (9600 cells), `F2` (double resolution, 19200 cells), and `L` (two times coarser resolution, 4800 cells) are shown together with the model `ND` where photon diffusion along the

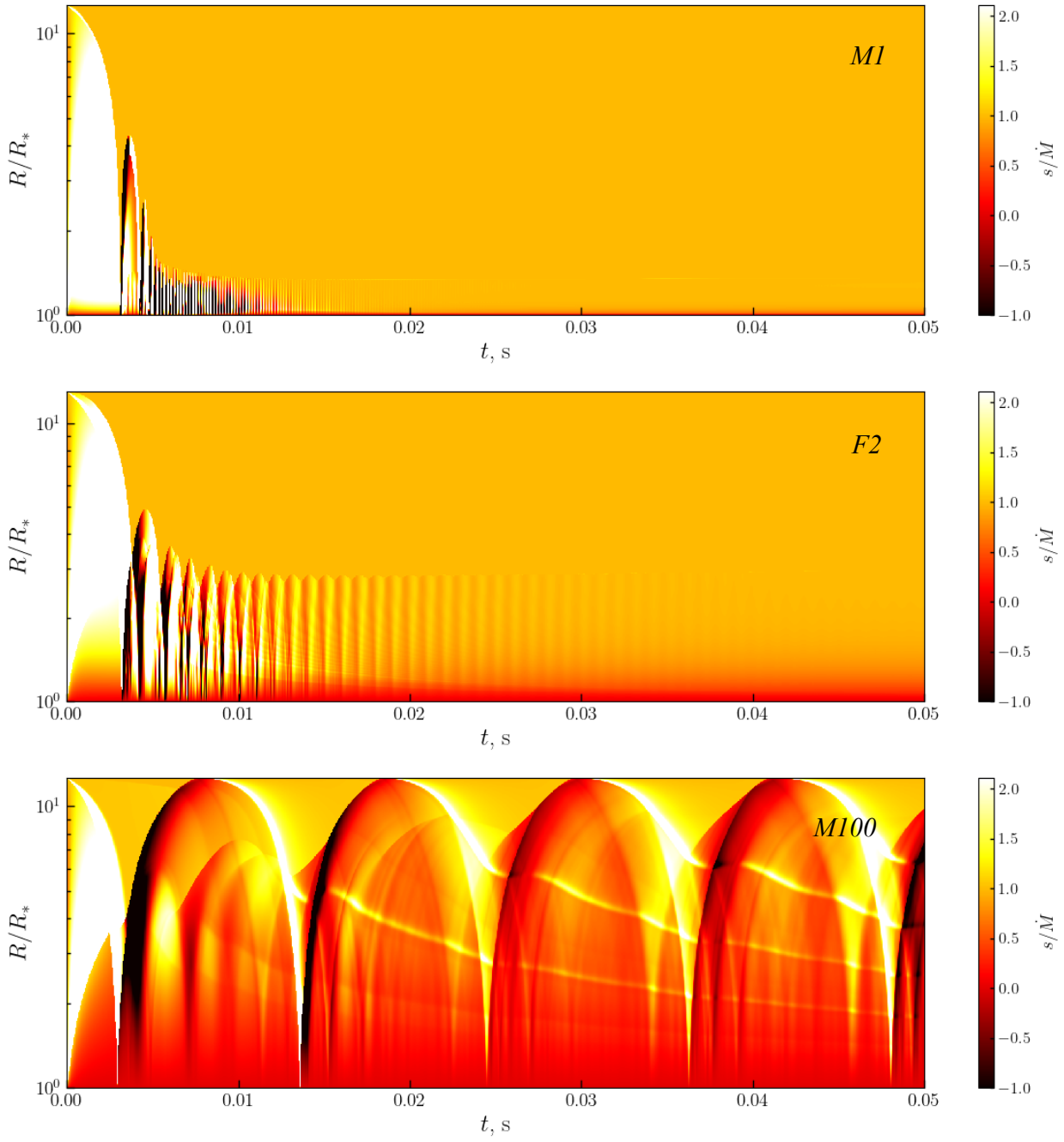

Figure 4. Local mass accretion rate plotted as a function of radius and time for three models (`M1`, `F`, and `M100`). Only the first 0.05s of evolution are shown.

field lines is turned off. As we can see in the plot, the overall structure remains practically independent of resolution, which argues for the stability and reliability of the algorithm.

Taking into account photon diffusion affects the shock position only slightly, by an amount comparable to the mean free path of a photon. The profiles of all the physical quantities close to the shock front clearly change. The flow structure away from the shock, however, remains practically unaffected. In general, photon diffusion is most important on the spacial scales of the photon mean free path ($\sim 1/\varkappa\rho$). In Fig. 9, we show the optical depth along the field line $\tau = \int \varkappa\rho \mathrm{d}l$ as a secondary axis. As we can see, the main effect of photon diffusion is the penetration of some of the energy into the upstream region, up to the depths of several. This agrees qualitatively with the picture drawn by the theory of radiation-mediated shock waves in the diffusion approximation (Zel'dovich & Raizer 1967; Levinson & Nakar 2020).

The effective temperature distribution in the optically thick part of the flow (see Fig. 9) suggests a thermal spectrum with a characteristic temperature of $T \sim 1 - 3$ keV. However, a rigorous calculation of the observed spectrum should involve a complex combination of visibility conditions (different viewing angles and self-occultations for different parts of the flow). Besides, radiation coming from a NS

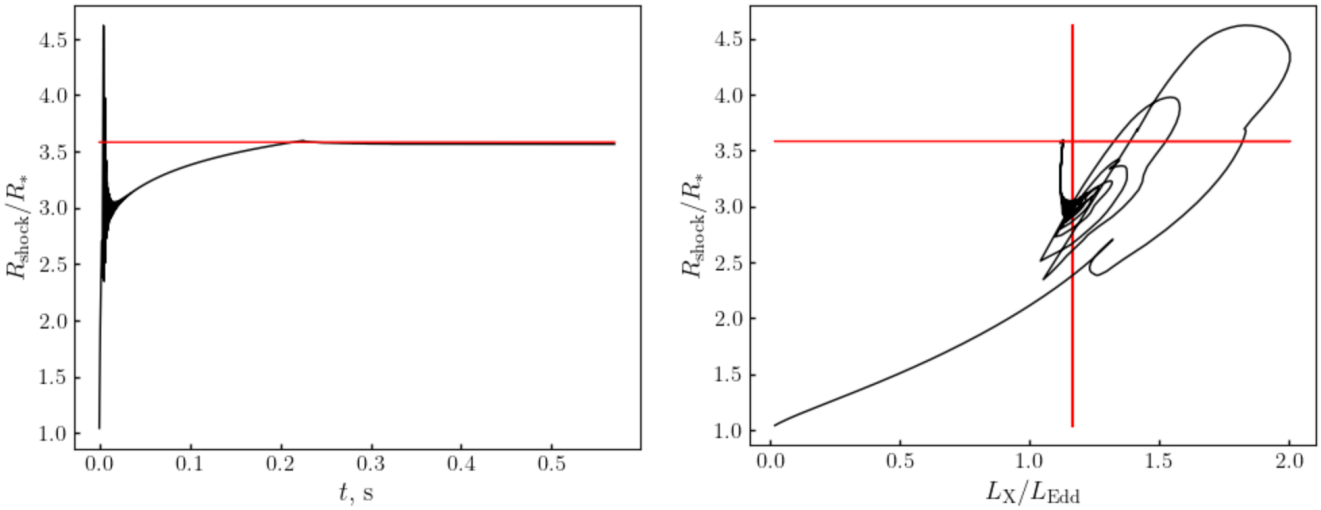

Figure 5. Shock position as a function of time (left panel) and luminosity $L_{\rm X}$ emitted below the shock (right panel) for model `B`. Shock position predicted by BS is shown with a horizontal red line, and the predicted luminosity is shown with a vertical red line in the right panel.

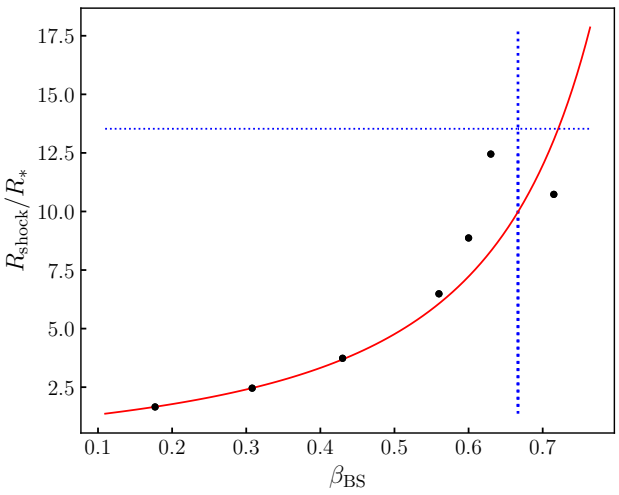

Figure 6. Shock front position as a function of $\beta_{\rm BS}$, shown for models `M100W2x` and `M100W3-50`, differing in $\Delta R_{\rm e}/R_{\rm e}$ (black dots). Predictions of the analytic model (equations 48 and 52) are shown with a red line. Vertical and horizontal blue dotted lines show the critical value $\beta_{\rm BS} = 2/3$ and the size of the magnetosphere.

accretion column should be strongly Comptonised. This Comptonisation may be saturated and non-saturated in different parts of the flow (see for example, West et al. 2017b). Modelling the observational properties of accretion columns is left to a separate paper.

For the fiducial model `F`, the transverse optical depth in the immediate upstream region is about several. The optical depth of a single resolution element along the field line is in most of the models smaller than unity. At such spatial scales, the diffusion approximation is no longer valid, as photons can cross multiple resolution elements freely between scatterings. More elaborate description of the radiation fields near the shock front would reveal an additional narrow 'Zeldovich spike' in energy density and temperature (see Tolstov et al. 2015; Fukue 2019 and references therein, and also Zel'dovich & Raizer 1967, Chapter VII).

3.5.2 *Irradiation and rotation*

In models `I`, `WI`, and `WI1`, irradiation is included in momentum and energy equations as a force opposing gravity (see equations 26, 27, and 31). We neglect the heating effect of irradiation. Physically, this corresponds to the case when all the irradiating energy flux is immediately isotropically scattered. Self-irradiation in the form adopted in our paper is not fully self-consistent: the irradiating source is assumed to be located in the origin and radiate isotropically, though its luminosity is calculated by integrating the radiative losses from the simulated flow. Also, the radiation scattered from the flow is not included in the irradiating luminosity. As long as most of the radiation losses occur near the NS surface, this is an accurate approximation in the outer magnetosphere.

Irradiation mostly influences the outer parts of the flow, decreasing the infall velocity. This decreases the energy release in the column and thus, somewhat counter-intuitively, the height of the column (Fig. 10). For $\eta_{\rm irr} = 0.5$, the shock shifts by less than one per cent. Increasing $\eta_{\rm irr}$ to the value of unity in `WI1`, in addition to the overall shift of the shock front, makes the position of the shock unstable and excites oscillations on short time scales. Probably, the nature of the oscillations is the same as the damped oscillations seen in all the models during their approach to equilibrium. However, irradiation adds an additional positive feedback that compensates the dissipation of the oscillations. The shock position given in Table 2 for `WI1` is a time-averaged value, and the uncertainty here is dominated by the motion of the shock front rather than by the size of the spatial resolution element, as in the fiducial model.

In models `R` and `RI`, we took into account centrifugal potential, tuned to match 0.9 Keplerian rotation rate at $R_{\rm e}$. The main effect is the decrease in power released below the shock. Adding irradiation to rotation, surprisingly, leads to a larger luminosity and higher shock front position, which is probably related to the amount of energy lost in the sink.

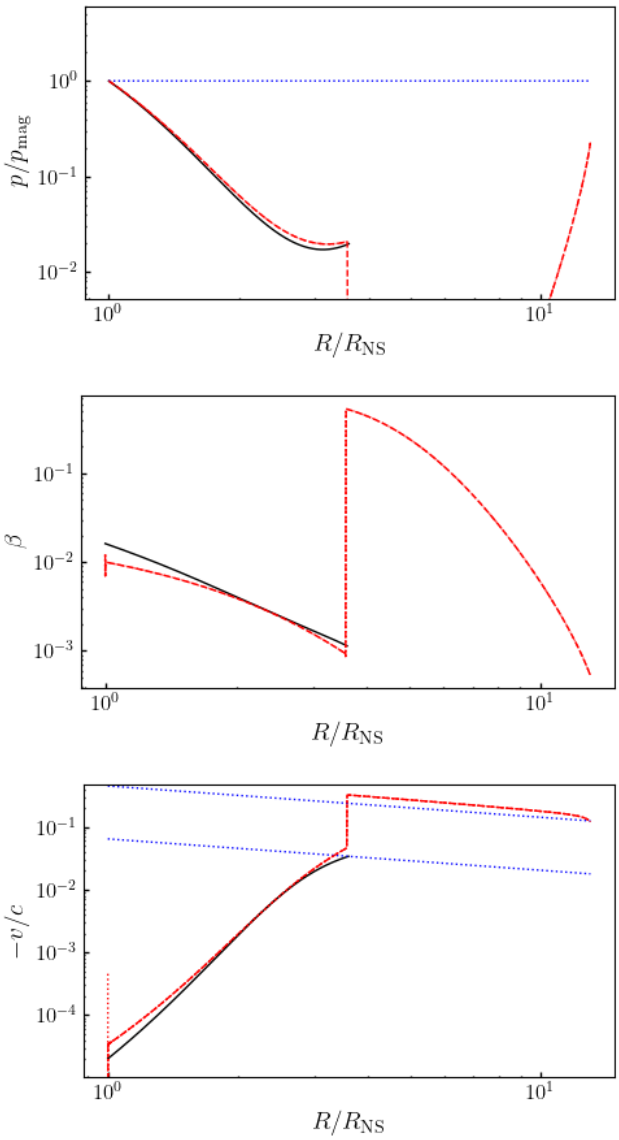

Figure 7. Stationary analytic solution (black solid lines) compared with our model B, averaged over the period of time 1.1 – 1.9 s. Upper panel: pressure normalised by the local magnetic field pressure. Blue dotted line shows the $p = p_{\rm mag}$ condition. Middle panel: gas-to-total pressure ratio. Lower panel: radial velocity. Blue dotted lines in the lower panel are Keplerian velocity $v_{\rm K}$ and $v_{\rm K}/7$.

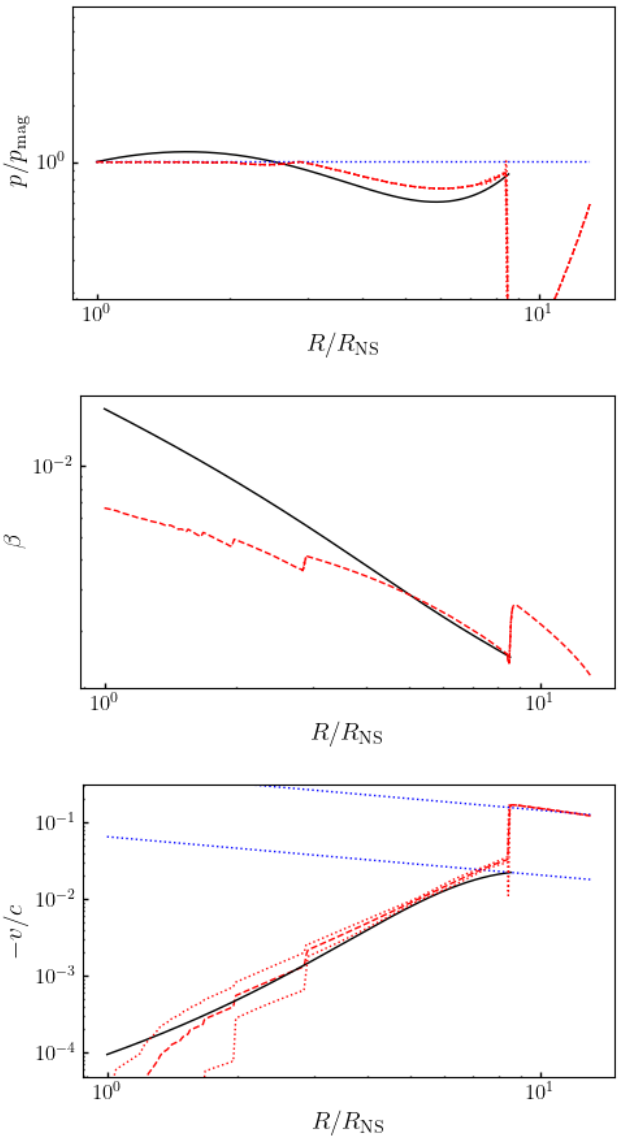

Figure 8. The same as previous figure, but for the model N2. Averaging was done over the time range 0.3 – 0.38 s. Red dotted lines show the variation limits of the time-dependent solution (mean value plus/minus one standard deviation).

3.6 Variability

An interesting feature of practically all the simulations is their oscillatory behaviour during the shock settling stage. In all the simulations with radiation diffusion included, the position of the shock shows damped oscillations with a frequency close to the expected dynamical frequency at the relevant height. For example, for the fiducial model, oscillations are present while the shock front position changes in the range $R_{\rm shock} \sim 2 - 5\ R_*$, where the expected dynamical frequency is $f_{\rm dyn} \simeq \frac{1}{2\pi}\sqrt{\frac{GM_*}{R^3_{\rm shock}}} \sim 200 - 800$ Hz. If this interpretation is correct, moving shock position will result in a frequency shift. This is difficult to check if the dynamical and replenishment time scales differ only by a factor of several, as in model F.

Simulation H has a larger magnetosphere size and hence a larger difference between the dynamical and replenishment time scales, allowing us to track the evolution of the oscillations during the settling of the shock front. In Fig. 11, we show a temporally resolved power-density spectrum (PDS) for the total luminosity (calculated according to equation 37) during the first 0.5 s of evolution. For each time bin, the PDS is calculated as the square of the absolute value of the Fourier image of $L_{\rm tot}$, normalised using Miyamoto normalisation (Miyamoto et al. 1991; Nowak et al. 1999)

$$PDS = 2\left|\frac{\int L(t)\,{\rm e}^{-2\pi {\rm i} f t}\,{\rm d}t}{\int L(t)\,{\rm d}t}\right|^2, \qquad (55)$$

where f is linear frequency. For the larger portion of this time span, the radiation is highly variable at hectohertz frequencies. Most of the variability power is associated with the general settling trend,

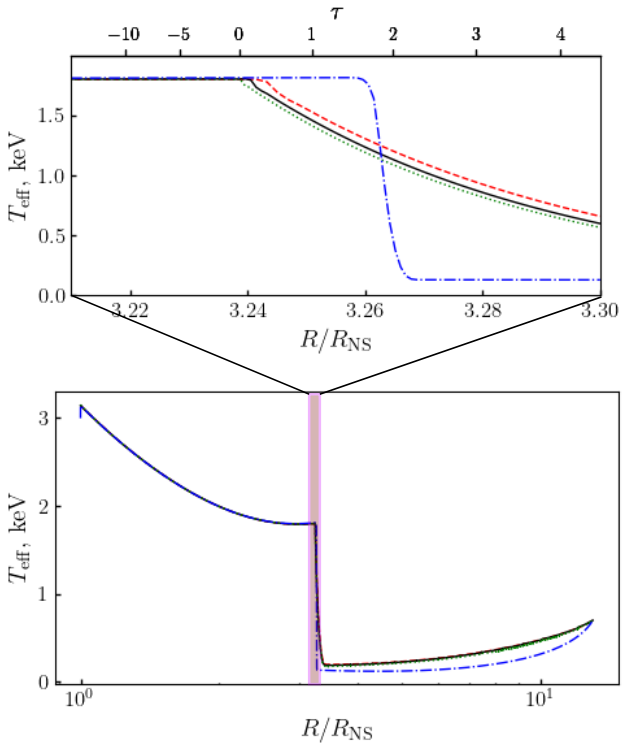

Figure 9. Effective temperature as a function of radius in models `F` (black solid curve), `L` (red dashed), `F2` (green dotted), and `ND` (blue dot-dashed). Upper panel shows a zoom-in into the shock region. The secondary x axis of the upper panel shows the optical depth along the field line (calculated for the model `F2`), with the zero point at the shock front position.

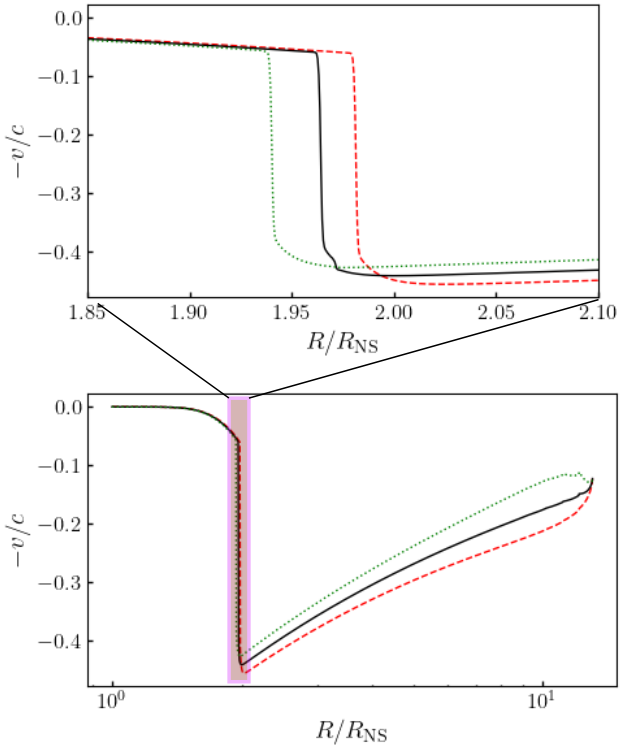

Figure 10. Time-averaged velocity dependence on radius for the models `W` (red dashed curve) , `WI` (black solid), and `WI1` (green dotted). Averaging was done over the last 10 per cent of the simulation time. As in Fig. 9, the lower panel shows the entire range of radii, and the upper panel zooms into the shock front region.

having a red spectrum with $PDS \propto f^{-2}$. Hence, in Fig. 11, we show $f^2 PDS$, and the position of the peak in the spectrum is found as the maximum of this combination. This maximum evidently corresponds to a damped oscillation mode with an amplitude of about several per cent and a frequency changing with time from about 200 to 500−600 Hz, as the shock moves downwards.

The observed peak frequencies may be reproduced by calculating the time needed for a sound wave to propagate from the top of the column to its base and back. Let us consider an accretion column in dynamic equilibrium, with a structure identical to the solution of BS in everything save the lower boundary condition (as the energy density has not necessarily reached the breakdown limit). The time needed to travel between R_* and $R_{\rm shock}$ is, according to equations (5) and (7),

$$\Delta t_{\rm s} = \int_{\rm R_*}^{R_{\rm shock}} \frac{\sqrt{3\cos^2\theta + 1}}{2\cos\theta} \frac{{\rm d}R}{c_{\rm s}}, \tag{56}$$

where

$$c_{\rm s} \simeq \sqrt{\frac{4}{9}\frac{u}{\rho}} \simeq \sqrt{\frac{1}{3}\frac{GM_*}{R_*} e^{\gamma\xi} \left(\frac{1}{\xi}{\rm E}_2\left(\gamma\xi\right) + \beta_{\rm BS} e^{-\gamma} - {\rm E}_2\left(\gamma\right)\right)}, \tag{57}$$

and $\xi = R/R_*$. While γ depends only on geometry, $R_{\rm shock}$ and $\beta_{\rm BS}$ vary with time as they depend on the value of u at the NS surface. In the right panel of Fig. 11, the corresponding frequency $f_{\rm s} = 1/\Delta t_{\rm s}$ is shown for comparison. As $\Delta t_{\rm s}$ is the time needed for the sound to propagate only in one direction, from the shock front to the surface (or back), the oscillation mode we see in the simulations is likely the first overtone.

Apart from the main oscillation frequency, gradually changing with time, it is possible to detect its first two harmonics, with the frequencies two and three times larger (see the left panel of Fig. 11). Their amplitudes are at least one order of magnitude smaller, and they are less likely to be detectable in real astrophysical sources. Damping of the oscillations is likely physical rather than numerical, as its rate is about the same for different resolutions.

The flow does not approach a steady state after multiple replenishment times only for the models `N2` and `M100`, where the analytic solution is self-inconsistent, and in the model `WI1`, where irradiation apparently supports the oscillation process. For `N2` and `M100`, mass loss also varies with the oscillation phase, by about 20 per cent and by more than an order of magnitude, respectively.

4 DISCUSSION

4.1 Matter lost from the column

Introducing the mass-loss law (equation 24), we assumed that, whenever thermal pressure significantly exceeds the pressure of the magnetic field, mass is lost from the column at about the speed of sound. This leakage carries away also internal energy and momentum. This is a simplified picture, but it helps justify the inner boundary condition and extend the approach of BS to the parameter range where their solutions become internally inconsistent (see section 3.4).

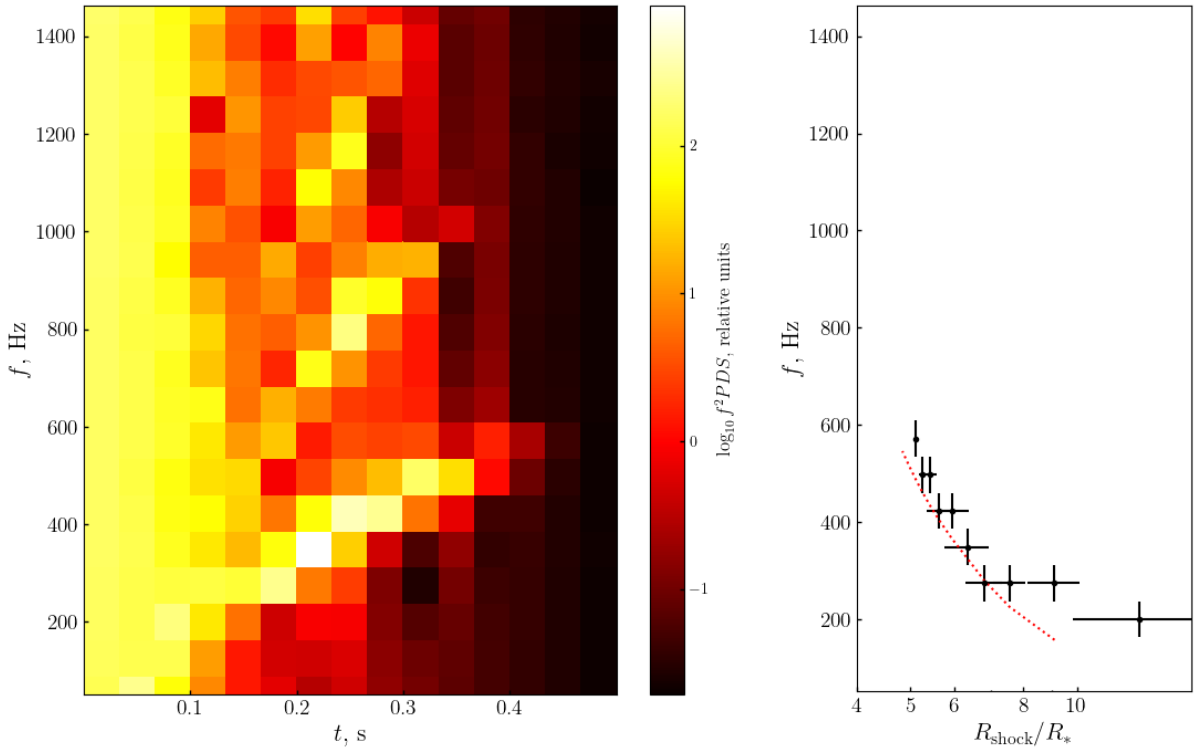

Figure 11. Left panel: dynamic power-density spectrum ($f^2 PDS$) for 15 uniform-length time intervals between $t = 0$ and 0.5 s, model `H`. Right panel: peak frequency for the same time bins as a function of shock position. Dynamical sound-travel frequency f_s is shown in the right plot with the red dotted line.

For moderate mass accretion rates (more precisely, for moderate advection parameters $\beta_{\rm BS} < 2/3$), accretion column tends to leak at the bottom. The physics behind this process involves three-dimensional interchange instabilities (Arons & Lea 1976) that start working when thermal pressure starts exceeding that of the magnetic field or a critical value scaling with the magnetic field pressure (Litwin et al. 2001; Mukherjee et al. 2013; Kulsrud & Sunyaev 2020). The matter leaving the column ultimately cools down and spreads over the surface of the NS (Melatos & Phinney 2001).

Large advection parameters cause the column to leak at a finite height. If a small amount of plasma leaves the column at a considerable height, it becomes immersed in a strong, super-Eddington, anisotropic external radiation field. Depending on the structure of the radiation field, the matter leaving the column may be either accreted or expelled along the field lines. We expect the realistic picture to be a combination of the three possible outcomes: (i) the cross-section of the column increases closer to the surface of the star, as the matter is spread over adjacent field lines; (ii) plasma is lost from the column onto closed magnetic field lines, and remains trapped inside the magnetosphere; (iii) plasma is ejected along the open field lines, acquiring mildly relativistic velocities.

If all the matter remains gravitationally bound but spreads onto adjacent field lines, the column may be considered as having larger cross-section and perimeter. Depending on the initial shape of the magnetospheric flow and the instability increments in different parts of the perimeter, effective $\beta_{\rm BS}$ may change differently. Increasing δ leads to larger $\beta_{\rm BS}$, while increasing azimuthal size decreases the effective value of $\beta_{\rm BS}$. If both the latitudinal and the longitudinal dimensions of the column increase by the same small amount of h, both thickness δ and cross-section $A_\perp$ increase linearly with h. This implies decreasing ratio $A_\perp/\delta^2$, smaller γ (equation 50), and larger $\beta_{\rm BS}$ (equation 52). Isotropic expansion of the column in general leads to smaller perimeter to cross-section ratio and, consequently, complicates cooling.

If the column has full azimuthal coverage ($a = 1$), the cross-section grows without any changes in the perimeter length. This is well illustrated by the sequence of models `M100W3-50`, that differ only in the latitudinal extent of the flow, set by the penetration depth at the outer boundary $\Delta R_{\rm e}$. Here, larger $\delta(R_*)$ leads to larger advection parameters. As longitudinal spreading of the column decreases the perimeter to cross-section ratio, it hinders the cooling of the column, leading to even larger effective values of $\beta_{\rm BS}$ and more spreading. One might check that increasing $\Delta R_{\rm e}$ in this case always leads to a decrease in γ and an increase in $\xi_{\rm s}$. According to equation (52), this leads to larger values of $\beta_{\rm BS}$.

The mass lost to the closed lines is likely to be trapped in certain regions of the magnetosphere and accumulate until its optical depth becomes larger than unity. Large optical depth decreases the contribution of the radiation pressure force and allows the matter to fall onto the star. The mass trapped on closed field lines is potentially a source of stochastic or quasi-periodic variability on the dynamical time scales of the outer magnetosphere (Abolmasov & Biryukov 2020).

The mass lost along the open field lines will likely acquire mildly relativistic velocities weakly dependent on the Eddington factor. If the Eddington limit is strongly violated, acceleration of the optically thin material is

$$\frac{{\rm d}v}{{\rm d}t} \simeq \frac{\varkappa L}{4\pi c R^2}. \qquad (58)$$

After integration along the approximately radial trajectory starting

from $R \simeq R_*$, this results in

$$v_{\rm out} \simeq \sqrt{\frac{\varkappa L}{4\pi c R_*}} = \sqrt{\frac{L}{L_{\rm Edd}} \frac{GM_*}{R_*}} \simeq 0.4 \sqrt{\frac{L}{L_{\rm Edd}} \frac{M_*}{1.4\,{\rm M}_\odot} \frac{11\,{\rm km}}{R_*}}\, c. \tag{59}$$

This provides XRPs with a mechanism to launch mildly relativistic outflows. If the outflow velocity becomes relativistic, the efficiency of the radiation pressure acceleration rapidly decreases, and Compton drag becomes important, making it essentially impossible to accelerate a flow by radiation pressure to velocities $\gtrsim 0.5c$ (Phinney 1982). Besides, non-negligible optical depth of the flow itself will decrease the effective luminosity value.

The electron-scattering optical depth of such an outflow (if not strongly collimated) is

$$\tau_{\rm out} \sim \int_{R_*}^{+\infty} \frac{\varkappa \dot{M}_{\rm out}}{4\pi R^2 v(R)}\, {\rm d}R \simeq \frac{c}{v_{\rm out}} \frac{\dot{M}_{\rm out} c^2}{L_{\rm Edd}} \gtrsim 1, \tag{60}$$

where $\dot{M}_{\rm out}$ is the mass-loss rate. Favourable (face-on) orientation of the source will allow to see the X-ray radiation of the central source through the outflowing matter. In this case, the observer will see blueshifted absorption features similar to those observed in some ultraluminous X-ray sources (Pinto et al. 2016; Kosec et al. 2018; Pinto et al. 2021).

Both black hole and NS accretors are likely to launch outflows with the velocities of the order of tenths of the speed of light, as this is the characteristic virial velocity in both cases. In particular, such outflows may be formed in the magnetospheres of highly magnetised NSs. Existence of a mildly relativistic outflow does not necessarily imply an accretion disc close to the compact object.

4.2 High-frequency oscillations of accretion columns

Our simulations clearly show an oscillation mode at the sound propagation time scale of the accretion column (see section 3.6). At the same time, in the observational data for real X-ray pulsars, there is little evidence for high-frequency ($\sim 100 - 1000$Hz) variability. The timing behaviour of the classic X-ray pulsars (long-spin-period accreting NSs in HMXB) is usually consistent with the assumption of all the variability coming from the accretion disc and maybe the outermost parts of the magnetosphere (Revnivtsev et al. 2009; Reig & Nespoli 2013). The frequency range above several tens of hertz is usually not covered due to poor statistics and interference from dead-time effects. In particular, for *RXTE/PCA*, dead time becomes an important factor at frequencies about 1kHz (Jahoda et al. 2006; Revnivtsev et al. 2015).

The 'bursting pulsar' GRO J1744−28 (D'A`i et al. 2015) shows a broad-band peaked noise component at hectohertz frequencies. In Klein et al. (1996), this variability component is interpreted as a manifestation of the photon bubble instability (Arons 1992) in the accretion column of the pulsar. Given the uniqueness of this object, it is hardly representative of the population of XRPs in general.

Probably, the only example of a conventional XRP with a reported detection of high-frequency variability is Cen X-3. It is a high-mass X-ray binary consisting of an OB donor star (Rappaport & Joss 1983) and a NS with the magnetic field of $(2-3)\times10^{12}$ G (measured using a cyclotron line, see Santangelo et al. 1998). The deep timing study performed by Jernigan et al. (2000) revealed a broad spectral feature at about 1kHz. While in the original paper this high-frequency variability was interpreted as a manifestation of the photon bubble instability, its properties are also consistent with the global oscillations of an accretion column. The luminosity ($L \sim 10^{38}$ erg s^{-1}) and the magnetic field of the object (magnetic moment $\mu \sim 3\times10^{30}$ G cm^3) suggest the shock is located at $R_{\rm shock} \sim 2R_*$, and the sound propagation time is $10^{-4} - 10^{-2}$ s, depending on the details of the geometry. However, the results reported by Jernigan et al. (2000) are questionable because of the interfering instrumental effects, that are likely to produce excess power around ~ 1 kHz. The possible timing artefacts were considered by Revnivtsev et al. (2015), who show that the spectral shapes of XRPs are unfavourable for timing studies at high frequencies, at least using *RXTE* data.

In accreting millisecond X-ray pulsars (AMXP, see Patruno & Watts 2021 for review), there is significant variability at the time scales comparable to the dynamical time scales near the surface of the accreting NS (van Straaten et al. 2005). For instance, they are known to have quasi-periodic oscillations (QPOs) in the hecto- and kilohertz range, similar to those observed in atoll sources (Wijnands & van der Klis 1999; van Straaten et al. 2005). However, luminosities of AMXPs rarely exceed 10^{37} erg s^{-1}, which practically excludes the formation of a radiation-dominated accretion column. AMXPs are known to have compact magnetospheres ($R_{\rm e}/R_* \lesssim 5$). The critical luminosity required for column formation L^*, according to the equation (1) of BS and formulae from our Appendix A, may be estimated for such objects as

$$L^* \sim a \sqrt{\frac{R_*}{R_{\rm e}}}\, L_{\rm Edd} \sim 10^{38}\,{\rm erg\,s^{-1}}. \tag{61}$$

Rapid variability of AMXPs, in many aspects similar to the variability of non-magnetised NSs, is probably related to the inner disc or boundary layer rather than to a magnetic column (van der Klis 2000).

The QPO seen in our simulation H has a large quality factor (probably larger than 10, see Fig. 11), and its frequency is a strong function of the luminosity of the column. This is a direct consequence of the one-dimensional nature of our simulations: all the parameters depend only on a single spatial coordinate, implying a single sound propagation time between the shock wave and the surface of the star. A realistic, multi-dimensional accretion column is unlikely to have a single shock front position for all the field lines, and the sound propagation times along different field lines should differ accordingly. Hence we suggest that, instead of a narrow QPO peak, a realistic accretion column should have a broad-band peaked noise excess in its PDS.

Qualitatively similar oscillations of the shock front were found in numerical simulations of accretion columns in T Tau stars (Koldoba et al. 2008) and cataclysmic variables (Bera & Bhattacharya 2018). The physical conditions in both cases are, however, different from the accretion columns in NS systems. In particular, accretion columns formed during accretion onto young stars and white dwarfs are usually optically thin. Thus, radiation pressure is usually a minor factor. The oscillations found by Bera & Bhattacharya (2018), involving weak secondary shocks propagating between the surface of the accretor and the primary shock front, also have a period well approximated by the sound crossing time scale. Interestingly, certain magnetic cataclysmic variables indeed have oscillation modes at about 1 Hz, suggestive for the column oscillation times. A comprehensive list of magnetic CVs showing QPOs with frequencies ~ 1 Hz is given by Bonnet-Bidaud et al. (2015).

4.3 Observability of the replenishment time scale

As we have seen in section 2.2, column replenishment time scales in most XRPs should be longer than the dynamical times at the magnetosphere boundary. At the same time, most of the energy emitted by a rapidly accreting XRP normally comes from the accretion column.

Does this mean that all the variability of the disc at the time scales shorter than the replenishment time will be damped? This is an issue we are planning to address in a separate paper.

It is well known that the power density spectra of X-ray pulsars have a break at a frequency close to the spin frequency of the NS. The position of the break changes with time and apparently correlates with the flux (Revnivtsev et al. 2009). If the break frequency corresponds to the dynamical time scale at the radius of the magnetosphere, we expect $f_{\rm break} \propto \dot{M}^{3/7}$. However, if the spectrum is cut off at the replenishment time, we expect a different scaling $f_{\rm break} \propto \dot{M}^{5/7}(\Delta R_{\rm e}/R_{\rm e})^{-1}$, involving the variations of the penetration depth in addition to the magnetosphere radius. For typical X-ray pulsar parameters, we also expect the values of the break frequency to be smaller if related to the replenishment time.

An important observational test for replenishment time would be to track the transition from the accretor to the propeller stage. However, this transition should occur at a luminosity large enough to support an accretion column, presumably above $\sim 10^{36} - 10^{37}\,{\rm erg\,s^{-1}}$ (equation 61). On the other hand, transition between accretor and propeller states occurs in a wide range of luminosities $L \sim 10^{35} - 10^{37}$ (Cui 1997; Campana et al. 2001; Tsygankov et al. 2016). Most relevant candidate events are the two turn-off transitions observed for 4U 0115+63 and V 0332+53 (Tsygankov et al. 2016). Observational data allow one to estimate the flux decrease time scales during these events as about 14.3 and 5.6 hours, respectively.

For an XRP with the spin period $P_{\rm s} = 2\pi/\Omega$, replenishment time scale may be estimated by substituting $\xi_{\rm m} R_{\rm A} = \left(GM/\Omega^2\right)^{1/3}$ to (10), in the assumption that the size of the magnetosphere coincides with the co-rotation radius $(GM/\Omega^2)^{1/3}$. Finally, we get

$$t_{\rm r} = (2\pi)^{-2/3}\frac{a}{2^{1/6}}\frac{\Delta R_{\rm e}}{R_{\rm e}}\xi_{\rm m}^{-8/3}\frac{(GM_*)^{1/3}}{R_*}P_{\rm spin}^{5/3} \simeq 180\frac{a}{\xi_{\rm m}^{8/3}}\frac{\Delta R_{\rm e}}{R_{\rm e}}\left(\frac{M_*}{1.5\,{\rm M}_\odot}\right)^{1/3}\frac{10\,{\rm km}}{R_*}\left(\frac{P_{\rm spin}}{1{\rm s}}\right)^{5/3}{\rm s}. \quad (62)$$

Note the strong dependence on $\xi_{\rm m}$ allows the actual replenishment time to vary in broad limits, from seconds to hours. For the parameters of 4U 0115+63 (spin period $P_{\rm spin} \simeq 3.62$s, magnetic moment $\mu \simeq 10^{30}{\rm G\,cm^3}$), the above expression may be used to explain a process taking several hours. However, fast-decaying light curves are also expected to appear as a result of the evolution of a viscous accretion disc with a cooling front (see, for example, Lipunova et al. 2022).

5 CONCLUSIONS

Modelling the dynamics of a NS accretion column allows us to reproduce the main results of the analytic model of BS. In a broad range of parameter values, the analytic model accurately predicts the position of the shock. The structure of the sinking region below the shock is also well reproduced.

Analysing the consistency of the models at high mass accretion rates, we find a new and simple criterion that restricts the applicability of the analytic model: the advection parameter $\beta_{\rm BS}$, incorporating mass accretion rate and column geometry, should not exceed 2/3. At large mass accretion rates and optical depths, when radiative cooling becomes inefficient, the vertical pressure profile becomes shallower than the vertical profile for magnetic pressure. As a result, thermal pressure becomes dominant over magnetic pressure not at the base of the column, as it was assumed by BS, but at a finite height above the surface of the NS.

This conjecture, following from analytic considerations, is also supported by our numerical results. For the models with a large advected fraction of the accretion power (more than 2/3), mass loss tends to occur at a finite height, and agreement with the analytic solution is significantly worse.

Mass loss from a finite height should lead to deformation or spreading of the column (its transverse size becomes larger than expected from the dipole geometry of the problem), mass-loading of the closed field lines inside the magnetosphere or of the open field lines. Mass loading of the open field lines is a possible way to create mildly relativistic outflows from a magnetised accreting NS.

The characteristic time scale at which an accretion column evolves to the stationary solution may be described as the mass replenishment time. This is the time needed to accumulate enough mass to put the bottom of the column to the edge of a breakdown (thermal and magnetic pressures become equal). For a large magnetosphere, this time scale generally exceeds the dynamical time scale of the inner accretion disc, making it a potentially important feature in the variability spectra of XRPs.

In particular, finite lifetime of an accretion column may affect the behaviour during accretor-propeller transitions, if the transition occurs from the state with a radiation-supported accretion column.

We find that the approach to the equilibrium state is non-monotonic, showing damped oscillations of the shock front position around the average trend. The frequency of this oscillation mode corresponds to the sound propagation time between the shock wave and the NS surface. For actual XRPs, the frequency is in the hecto- to kilohertz range, which is difficult to study with the available telescopes, but a prospective target for the future generations of X-ray timing instruments.

ACKNOWLEDGEMENTS

We acknowledge the support from the Academy of Finland grants 332666 and 333112. The analytic solution's behaviour for tall accretion columns was supported by the Russian Science Foundation grant 21-12-00141 and performed in Moscow Lomonosov State University. The authors would like to thank Sergey Tsygankov and Amir Levinson for the valuable discussions about the timing of X-ray pulsars and about radiative shocks, respectively, and Evgeny Derishev for drawing our attention to the radiative nature of the shock. We acknowledge the use of `MayaVI` 3D-plotting software (Ramachandran & Varoquaux 2011).

DATA AVAILABILITY

The numerical code `HACol` is freely available on `https://github.com/pabolmasov/HACol`. All the simulation results are available upot request.

REFERENCES

Abarca D., Parfrey K., Kluźniak W., 2021, ApJ, 917, L31
Abolmasov P., Biryukov A., 2020, MNRAS, 496, 13
Arons J., 1992, ApJ, 388, 561
Arons J., Lea S. M., 1976, ApJ, 207, 914
Arons J., Klein R. I., Lea S. M., 1987, ApJ, 312, 666
Bachetti M., Romanova M. M., Kulkarni A., Burderi L., di Salvo T., 2010, MNRAS, 403, 1193
Bachetti M., et al., 2014, Nature, 514, 202
Basko M. M., Sunyaev R. A., 1975, A&A, 42, 311

Basko M. M., Sunyaev R. A., 1976, MNRAS, 175, 395
Becker P. A., 1998, ApJ, 498, 790
Becker P. A., Wolff M. T., 2007, ApJ, 654, 435
Bera P., Bhattacharya D., 2018, MNRAS, 474, 1629
Bildsten L., et al., 1997, ApJS, 113, 367
Bonnet-Bidaud J. M., Mouchet M., Busschaert C., Falize E., Michaut C., 2015, A&A, 579, A24
Brumback M. C., Hickox R. C., Fürst F. S., Pottschmidt K., Tomsick J. A., Wilms J., Staubert R., Vrtilek S., 2021, ApJ, 909, 186
Caballero I., Wilms J., 2012, Mem. Soc. Astron. Italiana, 83, 230
Campana S., Gastaldello F., Stella L., Israel G. L., Colpi M., Pizzolato F., Orland ini M., Dal Fiume D., 2001, ApJ, 561, 924
Chandrasekhar S., 1967, An introduction to the study of stellar structure
Courant R., Friedrichs K., Lewy H., 1967, IBM Journal of Research and Development, 11, 215
Cui W., 1997, ApJ, 482, L163
D'Aì A., et al., 2015, MNRAS, 449, 4288
Davidson K., 1973, Nature Physical Science, 246, 1
Einfeldt B., 1988, SIAM Journal on Numerical Analysis, 25, 294
Filippova E. V., Mereminskiy I. A., Lutovinov A. A., Molkov S. V., Tsygankov S. S., 2017, Astronomy Letters, 43, 706
Fukue J., 2019, MNRAS, 483, 2538
Fürst F., et al., 2016, ApJ, 831, L14
Harten A., Lax P., van Leer B., 1983, SIAM Rev, 25, 35
Inoue H., 1975, PASJ, 27, 311
Israel G. L., et al., 2017a, Science, 355, 817
Israel G. L., et al., 2017b, MNRAS, 466, L48
Jahoda K., Markwardt C. B., Radeva Y., Rots A. H., Stark M. J., Swank J. H., Strohmayer T. E., Zhang W., 2006, ApJS, 163, 401
Jernigan J. G., Klein R. I., Arons J., 2000, ApJ, 530, 875
Kaaret P., Feng H., Roberts T. P., 2017, ARA&A, 55, 303
Kawashima T., Mineshige S., Ohsuga K., Ogawa T., 2016, PASJ, 68, 83
Keshtiban I., Belblidia F., Webster M., 2003, Int. J. Numer. Methods Fluids, 23, 77
Klein R. I., Jernigan J. G., Arons J., Morgan E. H., Zhang W., 1996, ApJ, 469, L119
Koldoba A. V., Ustyugova G. V., Romanova M. M., Lovelace R. V. E., 2008, MNRAS, 388, 357
Kosec P., Pinto C., Walton D. J., Fabian A. C., Bachetti M., Brightman M., Fürst F., Grefenstette B. W., 2018, MNRAS, 479, 3978
Kretschmar P., et al., 2021, A&A, 652, A95
Kulkarni A. K., Romanova M. M., 2013, MNRAS, 433, 3048
Kulsrud R. M., Sunyaev R., 2020, Journal of Plasma Physics, 86, 905860602
Lamb F. K., Pethick C. J., Pines D., 1973, ApJ, 184, 271
Levinson A., Nakar E., 2020, Phys. Rep., 866, 1
Lipunova G., Malanchev K., Tsygankov S., Shakura N., Tavleev A., Kolesnikov D., 2022, MNRAS, 510, 1837
Litwin C., Brown E. F., Rosner R., 2001, ApJ, 553, 788
Melatos A., Phinney E. S., 2001, Publ. Astron. Soc. Australia, 18, 421
Miyamoto S., Kimura K., Kitamoto S., Dotani T., Ebisawa K., 1991, ApJ, 383, 784
Mukherjee D., Bhattacharya D., Mignone A., 2013, MNRAS, 435, 718
Mushtukov A., Tsygankov S., 2022, arXiv e-prints, p. arXiv:2204.14185
Mushtukov A. A., Suleimanov V. F., Tsygankov S. S., Ingram A., 2017, MNRAS, 467, 1202
Mushtukov A. A., Portegies Zwart S., Tsygankov S. S., Nagirner D. I., Poutanen J., 2021, MNRAS, 501, 2424
Nowak M. A., Vaughan B. A., Wilms J., Dove J. B., Begelman M. C., 1999, ApJ, 510, 874
Parfrey K., Tchekhovskoy A., 2017, ApJ, 851, L34
Parfrey K., Spitkovsky A., Beloborodov A. M., 2016, ApJ, 822, 33
Patruno A., Watts A. L., 2021, in Belloni T. M., Méndez M., Zhang C., eds, Astrophysics and Space Science Library Vol. 461, Astrophysics and Space Science Library. pp 143–208 (arXiv:1206.2727), doi:10.1007/978-3-662-62110-3_4
Phinney E. S., 1982, MNRAS, 198, 1109
Pinto C., Middleton M. J., Fabian A. C., 2016, Nature, 533, 64
Pinto C., et al., 2021, MNRAS, 505, 5058
Pintore F., Zampieri L., Stella L., Wolter A., Mereghetti S., Israel G. L., 2017, ApJ, 836, 113
Portegies Zwart S. F., Dewi J., Maccarone T., 2004, MNRAS, 355, 413
Poutanen J., Lipunova G., Fabrika S., Butkevich A. G., Abolmasov P., 2007, MNRAS, 377, 1187
Pringle J. E., Rees M. J., 1972, A&A, 21, 1
Raguzova N. V., Popov S. B., 2005, Astronomical and Astrophysical Transactions, 24, 151
Ramachandran P., Varoquaux G., 2011, Computing in Science & Engineering, 13, 40
Rappaport S. A., Joss P. C., 1983, in Lewin W. H. G., van den Heuvel E. P. J., eds, Accretion-Driven Stellar X-ray Sources. pp 1–39
Reig P., 2011, Ap&SS, 332, 1
Reig P., Nespoli E., 2013, A&A, 551, A1
Revnivtsev M., Churazov E., Postnov K., Tsygankov S., 2009, A&A, 507, 1211
Revnivtsev M. G., Molkov S. V., Pavlinsky M. N., 2015, MNRAS, 451, 4253
Rodríguez Castillo G. A., et al., 2020, ApJ, 895, 60
Romanova M. M., Ustyugova G. V., Koldoba A. V., Wick J. V., Lovelace R. V. E., 2003, ApJ, 595, 1009
Santangelo A., del Sordo S., Segreto A., dal Fiume D., Orlandini M., Piraino S., 1998, A&A, 340, L55
Scharlemann E. T., 1978, ApJ, 219, 617
Tikhonov A., Samarskii A., 2013, Equations of Mathematical Physics. Dover Books on Physics, Dover Publications, https://books.google.fi/books?id=PTmoAAAAQBAJ
Tolstov A., Blinnikov S., Nagataki S., Nomoto K., 2015, ApJ, 811, 47
Toro E. F., Spruce M., Speares W., 1994, Shock Waves, 4, 25
Tsygankov S. S., Lutovinov A. A., Doroshenko V., Mushtukov A. A., Suleimanov V., Poutanen J., 2016, A&A, 593, A16
Turkel E., 1999, Annual Review of Fluid Mechanics, 31, 385
Wang Y. M., Frank J., 1981, A&A, 93, 255
West B. F., Wolfram K. D., Becker P. A., 2017a, ApJ, 835, 129
West B. F., Wolfram K. D., Becker P. A., 2017b, ApJ, 835, 130
Wijnands R., van der Klis M., 1999, ApJ, 514, 939
Wolff M., et al., 2019, BAAS, 51, 386
Zel'dovich Y. B., Raizer Y. P., 1967, Physics of shock waves and high-temperature hydrodynamic phenomena
van Straaten S., van der Klis M., Wijnands R., 2005, ApJ, 619, 455
van der Klis M., 2000, ARA&A, 38, 717

APPENDIX A: GEOMETRY: TECHNICAL DETAILS

The field of a magnetic dipole is given by the general formula

$$\boldsymbol{B} = \frac{3(\boldsymbol{\mu}\cdot\boldsymbol{R})\boldsymbol{R}}{R^5} - \frac{\boldsymbol{\mu}}{R^3}, \tag{A1}$$

where $\boldsymbol{\mu}$ is the magnetic dipole moment vector. We assume the dipole to be aligned with the angular momentum in the accretion disc (considered only as a source of mass) and with the rotation of the NS. We also assume that the field lines retain their shapes (there is no significant back-reaction from the flow), and the matter follows the field lines. The geometry of the flow in these assumptions implies a simple relation valid for an aligned dipole in spherical coordinates $R = R_e \sin^2\theta$, where θ is the polar angle, and R is the spherical radial coordinate.

A unit vector along the field line

$$\boldsymbol{e}_l = \frac{2\cos\theta\,\boldsymbol{e}_R + \sin\theta\,\boldsymbol{e}_\theta}{\sqrt{3\cos^2\theta + 1}}, \tag{A2}$$

where $\boldsymbol{e}_R$ and $\boldsymbol{e}_\theta$ are the corresponding unit coordinate vectors. The cosine of the angle between the magnetic field and the radial unit vector is the scalar product of $\boldsymbol{e}_r$ and $\boldsymbol{e}_l$. Taking the scalar product

allows us to relate R and the coordinate along the field line l as

$$\frac{\mathrm{d}R}{\mathrm{d}l} = \frac{2\cos\theta}{\sqrt{3\cos^2\theta+1}}. \tag{A3}$$

The size of the flow perpendicular to the field line $\delta \ll R$ (width of the accretion curtain) may be calculated using flux conservation. Magnetic flux $|\boldsymbol{B}|\,A_\perp = const$, where $|\boldsymbol{B}| = \mu\sqrt{3\cos^2\theta+1}/R^3$ follows from equation (A1). The cross-section of the flux tube equals

$$A_\perp = 4\pi a R \sin\theta\delta, \tag{A4}$$

which implies

$$\frac{\delta}{R} = \frac{\sin\theta}{\sqrt{1+3\cos^2\theta}}\frac{\Delta R_\mathrm{e}}{R_\mathrm{e}}. \tag{A5}$$

The polar angle of the footpoint of a field line is given by the relation

$$\sin\theta_\mathrm{min} = \sqrt{R_*/R_\mathrm{e}}. \tag{A6}$$

Substituting this expression to (A5), we find the width of the accretion curtain at the surface

$$\delta_* = R_*\sqrt{\frac{R_*}{R_\mathrm{e}(4-3R_*/R_\mathrm{e})}}\frac{\Delta R_\mathrm{e}}{R_\mathrm{e}} \approx \frac{\Delta R_\mathrm{e}}{2}\left(\frac{R_*}{R_\mathrm{e}}\right)^{3/2}. \tag{A7}$$

The part of the NS surface occupied by the accretion flows is

$$\frac{A_{\perp,*}}{4\pi R_*^2} = \frac{a\,\delta_*}{\sqrt{R_* R_\mathrm{e}}} \approx \frac{a}{2}\frac{R_*}{R_\mathrm{e}}\frac{\Delta R_\mathrm{e}}{R_\mathrm{e}}. \tag{A8}$$

The approximations above hold if $R_* \ll R_\mathrm{e}$ and $\Delta R_\mathrm{e} \ll R_\mathrm{e}$. If the size of the magnetosphere is two orders of magnitude larger than the radius of the NS, $A_{\perp,*}$ is expected to be smaller than one per cent of the surface of the star.

The angle α between the magnetic line and horizontal direction may be found by considering the unit vector

$$\boldsymbol{e}_\varpi = \boldsymbol{e}_R\sin\theta + \boldsymbol{e}_\theta\cos\theta, \tag{A9}$$

directed along the radial direction of a cylindrical coordinate system. Scalar product $\boldsymbol{e}_\varpi \cdot \boldsymbol{e}_l$ allows one to calculate the angle α between the cylindric radial direction set by vector $\boldsymbol{e}_\varpi$ and the field line (see Fig. 1),

$$\cos\alpha = \frac{3\cos\theta\,\sin\theta}{\sqrt{1+3\cos^2\theta}}. \tag{A10}$$

The sign of α is assumed positive if the tangent to the field line makes an acute angle with the symmetry axis (as in Fig. 1). Note that α changes sign when $\cos\theta = 1/\sqrt{3}$. Centrifugal force, projected onto the field line, enters the momentum conservation equation with a multiplier of $\cos\alpha$. Gravity is directed along $\boldsymbol{e}_R$, hence its contribution to equation (26) should be multiplied by

$$\boldsymbol{e}_R \cdot \boldsymbol{e}_l = \sin(\alpha+\theta) = \frac{2\cos\theta}{\sqrt{1+3\cos^2\theta}}. \tag{A11}$$

APPENDIX B: GAS-TO-TOTAL PRESSURE RATIO

Pressure ratio β is defined as

$$\beta = p_\mathrm{gas}/p = \frac{p_\mathrm{gas}}{p_\mathrm{gas}+p_\mathrm{rad}}, \tag{B1}$$

where p_gas is gas pressure

$$p_\mathrm{gas} = \frac{\rho k T}{\tilde{m}}, \tag{B2}$$

$\tilde{m}$ is the mean mass of a particle, and

$$p_\mathrm{rad} = \frac{u_\mathrm{rad}}{3} = \frac{4}{3}\frac{\sigma_\mathrm{SB}}{c}T^4. \tag{B3}$$

For the gas constituent of pressure,

$$u_\mathrm{gas} = \frac{3}{2}p_\mathrm{gas} = \frac{3}{2}\frac{\rho}{\tilde{m}}kT. \tag{B4}$$

From equation (B3) we express the temperature as

$$T = \left(\frac{c\,u_\mathrm{rad}}{4\,\sigma_\mathrm{SB}}\right)^{1/4} = \left(\frac{c\,u}{4\,\sigma_\mathrm{SB}}\frac{1-\beta}{1-\beta/2}\right)^{1/4}, \tag{B5}$$

and substitute it to (B4) obtaining an equation for β, which may be solved given mass and energy density

$$\frac{\beta}{(1-\beta/2)^{3/4}\,(1-\beta)^{1/4}} = \frac{3}{\sqrt{2}}\frac{k}{\tilde{m}}\left(\frac{c}{\sigma_\mathrm{SB}}\right)^{1/4}\frac{\rho}{u^{3/4}}. \tag{B6}$$

This paper has been typeset from a TEX/LATEX file prepared by the author.